



Emission line models for the lowest mass core-collapse supernovae – I. Case study of a $9 M_{\odot}$ one-dimensional neutrino-driven explosion

A. Jerkstrand,¹ T. Ertl,¹ H.-T. Janka,¹ E. Müller,¹ T. Sukhbold² and S. E. Woosley³

¹Max-Planck Institut für Astrophysik, Karl-Schwarzschild Str 1, D-85748 Garching, Germany

²Department of Astronomy, Center for Cosmology & Astro-Particle Physics, The Ohio State University, Columbus, OH 43210, USA

³Department of Astronomy and Astrophysics, University of California, Santa Cruz, CA 95064, USA

Accepted 2017 November 3. Received 2017 November 2; in original form 2017 August 9

ABSTRACT

A large fraction of core-collapse supernovae (CCSNe), 30–50 per cent, are expected to originate from the low-mass end of progenitors with $M_{\text{ZAMS}} = 8\text{--}12 M_{\odot}$. However, degeneracy effects make stellar evolution modelling of such stars challenging, and few predictions for their supernova light curves and spectra have been presented. Here, we calculate synthetic nebular spectra of a $9 M_{\odot}$ Fe CCSN model exploded with the neutrino mechanism. The model predicts emission lines with $\text{FWHM} \sim 1000 \text{ km s}^{-1}$, including signatures from each deep layer in the metal core. We compare this model to the observations of the three subluminous IIP SNe with published nebular spectra; SN 1997D, SN 2005cs and SN 2008bk. The predictions of both line profiles and luminosities are in good agreement with SN 1997D and SN 2008bk. The close fit of a model with no tuning parameters provides strong evidence for an association of these objects with low-mass Fe CCSNe. For SN 2005cs, the interpretation is less clear, as the observational coverage ended before key diagnostic lines from the core had emerged. We perform a parametrized study of the amount of explosively made stable nickel, and find that none of these three SNe show the high $^{58}\text{Ni}/^{56}\text{Ni}$ ratio predicted by current models of electron capture SNe (ECSNe) and ECSN-like explosions. Combined with clear detection of lines from O and He shell material, these SNe rather originate from Fe core progenitors. We argue that the outcome of self-consistent explosion simulations of low-mass stars, which gives fits to many key observables, strongly suggests that the class of subluminous Type IIP SNe is the observational counterpart of the lowest mass CCSNe.

Key words: hydrodynamics – line: formation – radiative transfer – stars: evolution – supernovae: general – supernovae: individual: SN 1997D, SN 2005cs, SN 2008bk.

1 INTRODUCTION

Stars more massive than about $8 M_{\odot}$ end their evolution as core-collapse supernovae. Due to the steepness of the initial mass function (IMF), over 40 per cent of all CCSNe occur in the $8\text{--}12 M_{\odot}$ range and 25 per cent in the $8\text{--}10 M_{\odot}$ range. If a significant fraction of stars over $20 M_{\odot}$ would in addition fail to produce supernovae and collapse directly to black holes, the fraction in the $8\text{--}12 M_{\odot}$ range could be as high as 50–60 per cent (Sukhbold et al. 2016).

Stars in the $8\text{--}12 M_{\odot}$ range have a qualitatively different core structure than at $>12 M_{\odot}$, with significantly lower compactness (Sukhbold et al. 2016). They are typically easier to explode, and some explode even in 1D neutrino simulations (Kitaura, Janka & Hillebrandt 2006; Melson, Janka & Marek 2015; Radice et al. 2017). However, the evolution of such stars is more complex to model than at $>12 M_{\odot}$ due to degeneracy effects (see

e.g. Miyaji et al. 1980, for an early review). Thermal pulses develop that are numerically challenging to follow, and mass-loss is highly uncertain in the later phases. There have therefore been few models presented in the literature. This has in turn led to few models for their corresponding supernova light curves and spectra, and currently a fuzzy picture which observed events belong to this category.

The values of critical mass division points between final outcomes, between CO and ONe white dwarfs (WDs) (M_{up}), between ONe WDs and ECSNe (M_{n}) and between ECSNe and Fe CCSNe (M_{mas}) all shift by about $2 M_{\odot}$ with uncertain overshooting efficiencies (Siess 2007). There is also some dependence on metallicity (Umeda et al. 1999; Eldridge & Tout 2004). ‘Super-AGB’ stars represent the final phase for stars between M_{up} and M_{mas} that can end as either ONe WDs or ECSNe.

In the literature one finds values for M_{up} of $<9 M_{\odot}$ (García-Berro, Ritossa & Iben 1997), $7.5\text{--}9 M_{\odot}$ (Poelarends 2007) and $\leq 8.9 M_{\odot}$ (Siess 2007). There is close agreement in the necessary CO core mass needed to ignite carbon of $1.06 M_{\odot}$. Although

* E-mail: anders@mpa-garching.mpg.de

the value of M_n varies between studies (e.g. $8.7 M_\odot$ in Jones et al. 2013), there is close agreement in the predicted ONe core mass needed to produce an ECSN; $1.37 M_\odot$ (Nomoto 1984; Takahashi, Yoshida & Umeda 2013). For M_{mas} , values have been reported of $\geq 8.8 M_\odot$ (Nomoto 1984), $\geq 11 M_\odot$ (Ritossa, García-Berro & Iben 1999; Takahashi, Yoshida & Umeda 2013), $8.8 - 9.5 M_\odot$ (Jones et al. 2013), $9.25 M_\odot$ (Poelarends et al. 2008), $\leq 9 M_\odot$ (Woosley & Heger 2015) and $8.7 M_\odot$ (Siess 2007, with overshooting). Woosley & Heger (2015) also warn that the behaviour in this mass range is sometimes non-monotonic with mass, implying that such a grouping scheme may be oversimplified.

The mass range that theoretically leads to ECSNe, $M_n - M_{\text{up}}$, is relatively small, of order $1 M_\odot$ (Siess 2007). It is almost certainly not larger than $1.5 M_\odot$, and may be much smaller than $1 M_\odot$ (Poelarends et al. 2008; Doherty et al. 2015) or non-existent, depending on uncertainties in mass-loss and 3d dredgeup. An interval width of $1 M_\odot$ still corresponds to 15 per cent of all CCSNe with a standard Salpeter IMF, dropping to 8 per cent for $0.5 M_\odot$. An important current research topic is whether ECSNe exist at all, and if so, what fraction of CCSNe they constitute.

Progenitor structures at the point of core collapse for ECSNe have been calculated by Nomoto (1984, 1987), Takahashi, Yoshida & Umeda (2013) and Jones et al. (2013). Models halted earlier, but predicted to evolve to ECSNe, have been calculated by Ritossa, García-Berro & Iben (1996), García-Berro, Ritossa & Iben (1997), Iben, Ritossa & García-Berro (1997), Ritossa, García-Berro & Iben (1999), Siess (2006) and Woosley & Heger (2015). In these models the He layer has typically been reduced to almost nothing by a second dredge-up/dredge-out (Nomoto 1987; Ritossa, García-Berro & Iben 1996). The ONe core is surrounded by a thin O/C shell of mass a few $\times 0.01 M_\odot$, followed by a dilute H/He envelope. As the ONe core and part of the O/C shell collapse to a neutron star, the outer O/C shell gets burnt to iron-group elements (Mayle & Wilson 1988; Kitaura, Janka & Hillebrandt 2006; Janka et al. 2008). Longer term simulation of the neutrino wind (Pleilani et al. 2015) indicated no major modifications to the yields obtained after the explosive phase (Wanajo et al. 2009; Wanajo, Janka & Müller 2011). An important property of ECSNe from single-star progenitors is therefore that they have no O-rich shell in the ejecta, and also no He shell. The spectrum of such an event will be that of a H/He envelope, plus possibly signatures of explosively made iron-group elements. It is unclear whether the innermost Fe-rich layer is massive enough to be seen against the $\sim 8 M_\odot$ H/He envelope emission. If it is, the unusually high neutron excess may produce unique signatures, e.g. of stable nickel and zinc (Wanajo et al. 2009). Follow-up simulations in 2D demonstrated that for ECSNe dimensionality plays a relatively minor role for the dynamics but a more significant role for the nucleosynthesis (Janka et al. 2008; Wanajo, Janka & Müller 2011; Müller 2016).

For higher masses, neon may ignite degenerately in shell flashes (Nomoto 1984). These flashes may or may not propagate to the centre (Jones, Hirschi & Nomoto 2014). If they do, the star eventually forms an iron core. But O and Si also ignite quasi-degenerately, and it is unclear if these flashes may eject the outer layers of the star and maybe even prevent neutron star formation (Jones et al. 2016). Modern 1D models use subgrid flame propagation calculations, but a full understanding requires 3D simulations. These degenerate flashes occur up to about $10.3 M_\odot$, above which more normal non-degenerate evolution occurs (Woosley & Heger 2015). Recently a grid of iron core progenitors below $12 M_\odot$ was presented by Woosley & Heger (2015), who obtained iron core formation down to $9 M_\odot$.

Similar to ECSNe, the lowest mass iron CCSNe have steep density gradients outside their degenerate cores, and explode with similar energy and explosive nucleosynthesis (Janka et al. 2012; Müller 2016; Wanajo et al. 2017), although multi-D effects are here more important for the explosion energy (Melson, Janka & Marek 2015; Radice et al. 2017). This raises the question whether ECSNe and low-mass Fe CCSNe can be spectroscopically distinguished. The major distinction of the ejecta is that Fe core progenitors have layers of Si, O and (perhaps) He that, although thin, will not be fully burnt to iron-group elements, and may provide additional lines of Si, S, Ca, O, C, He to spectra. So ECSNe may be identified by lack of lines rather than presence of lines.

The main observational candidates for low-mass CCSNe are Type II SNe with low plateau luminosities and low expansion velocities, so-called subluminous Type IIP SNe. This class has about a dozen reasonably well-observed members, including SN 1997D (Turatto et al. 1998; Benetti et al. 2001), SN 2003gd (Hendry et al. 2005; Meikle et al. 2007), SN 2003Z (Spiro et al. 2014), SN 2004eg (Spiro et al. 2014), SN 2005cs (Pastorello et al. 2006, 2009), 2006ov (Spiro et al. 2014), SN 2008bk (Van Dyk et al. 2012; Maguire et al. 2012), SN 2008S (Botticella et al. 2009) and SN 2009md (Fraser et al. 2011). Pastorello et al. (2004) presented data on further candidates SN 1994N, SN 1999br, SN 1999eu and SN 2001dc. Of these, SN 1997D, SN 2005cs and SN 2008bk were spectroscopically observed at nebular phases ($t \gtrsim 200$ d). Recently, Tomasella et al. (2017) presented data on two additional events, SN 2013am and SN 2013K, that have properties between subluminous and normal IIP SNe.

Taking a more global view of the progenitors, strong mass-loss is expected in the super-AGB phase, e.g. for ECSN progenitors. Thus, this kind of SNe may conceivably become Type IIn SN. It is also possible that ECSNe and low-mass Fe CCSNe occur from He stars that have lost their H envelopes to a companion. In that case a Type Ib/c SN follows that is fast and very faint due to the low ejecta mass of $\sim 0.1 M_\odot$ (Tauris, Langer & Podsiadlowski 2015; Moriya & Eldridge 2016). The existence of such transients is difficult to establish due to the difficulty of detecting them.

Three of the subluminous IIP SNe (SN 2003gd, SN 2005cs and SN 2008bk) have progenitor detections, and these have all pointed to values in the $M_{\text{ZAMS}} = 8 - 15 M_\odot$ range. Van Dyk, Li & Filippenko (2003) estimated $M_{\text{ZAMS}} = 8 - 9 M_\odot$ for SN 2003gd. The optical disappearance of the progenitor could later be confirmed (Maund & Smartt 2009). Maund, Smartt & Danziger (2005) obtained $M_{\text{ZAMS}} = 9^{+3}_{-2} M_\odot$ for SN 2005cs, and Takáts & Vinkó (2006) found a similar estimate, with confirmed disappearance by Maund et al. (2014). Eldridge, Mattila & Smartt (2007) argued that upper limits in the NIR for SN 2005cs rule out a super-AGB progenitor, and thereby the possibility of an ECSN. Mattila et al. (2008) estimated $M_{\text{ZAMS}} = 8.5 \pm 1 M_\odot$ for SN 2008bk. The progenitor was later confirmed to have optically disappeared (Maund et al. 2014), with a revised progenitor mass estimate $M_{\text{ZAMS}} = 13 \pm 2 M_\odot$. Note that Fraser et al. (2011) identified a source with $M_{\text{ZAMS}} = 8.5^{+6.5}_{-1.5} M_\odot$ for SN 2009md, but this was later shown not to have disappeared and was thus not the SN progenitor (Maund et al. 2015).

Thus in three cases have subluminous IIP SNe been linked to the low-mass end of progenitors, all with confirmed optical disappearances. While the formation of optically thick dust clumps in SN ejecta may completely block out any surviving progenitor system in the optical, it is unlikely that this would have happened in all three cases as typically inferred covering factors are ~ 0.5 (e.g. Lucy et al. 1989). Any high-mass progenitor would also presumably have easily been detected, given the detection of low-mass

stars (although extinction is again a problem). Progenitor imaging therefore provides strong arguments against a scenario of high-mass progenitors for this class.

Light-curve modelling has also been undertaken. The first subluminous IIP SN, SN 1997D, was only observed from the very end of the plateau, and the plateau light curve itself can therefore not significantly constrain explosion models. However, both the low- and high-mass models initially proposed (Turatto et al. 1998; Chugai & Utrobin 2000) had short plateaus of 50–60d. Later on, SN 1997D-clones have been discovered that all have much longer plateaus ($\gtrsim 100$ d), and it is therefore likely that these original models are unsuitable.

Chugai & Utrobin (2000) demonstrated that at the conditions of high density and low ^{56}Ni mass, Rayleigh scattering has some effect on the photospheric spectral formation. Particularly for models with very high mass, this effect produced worsening of the spectral fits for SN 1997D, although the effects were quite minor. Zampieri et al. (2003) used a semi-analytic approach and favoured high ejecta mass ($14\text{--}17 M_{\odot}$) models for SN 1997D (now with assumed 110d plateau) and SN 1999br. Utrobin & Chugai (2008) found a high mass for SN 2005cs ($M_{\text{pre-SN}} = 17 \pm 2 M_{\odot}$) using advanced light-curve models, while Pastorello et al. (2009) found $M_{\text{pre-SN}} \sim 12 M_{\odot}$ with a semi-analytic approach. Spiro et al. (2014) found $M_{\text{pre-SN}} = 10 M_{\odot}$ for SN 2005cs and $M_{\text{pre-SN}} \sim 15 M_{\odot}$ for SN 2008in (a transitional object studied by Roy et al. 2011). Pumo et al. (2017) performed modelling for SN 2003Z, SN 2008bk and SN 2009md, estimating main-sequence masses in the $11\text{--}15 M_{\odot}$ range. Thus, light-curve modelling indicates $M_{\text{ZAMS}} \sim 10\text{--}20 M_{\odot}$, in dissonance with a hypothesis based on the progenitor imaging that these stars would come from 8 to $11 M_{\odot}$ progenitors.

The light-curve models described above do not simulate explosions of evolved progenitors, but use polytropes. Adding some focus on specific evolutionary models, Tominaga, Blinnikov & Nomoto (2013) computed light curves of thermal bomb explosions of H/He envelopes ($2.0\text{--}4.7 M_{\odot}$) attached to an ECSN progenitor core, using STELLA, and Moriya et al. (2014) extended this work to include circumstellar material (CSM) interaction. These two works pointed out that, with the very low ^{56}Ni mass, other energy sources such as a central pulsar or CSM interaction may dominate the light curve after a few hundred days.

A third modelling approach is spectral modelling, which is the topic of this paper. The last few years have seen the production of the first grids of spectral models for Type IIP SNe over M_{ZAMS} (Jerkstrand et al. 2012, hereafter J12; Dessart et al. 2013; Jerkstrand et al. 2014, hereafter J14). As demonstrated, e.g. for SN 1987A (Fransson & Chevalier 1989; Kozma & Fransson 1998a,b), models for the nebular phase of the SN allow diagnostics of the nucleosynthesis products, which produce emission lines that become distinct after about 200d. Constraints on these products allow inference of the progenitor, as well as on its explosive nucleosynthesis and mixing dynamics. However, these grids have so far only been computed down to $M_{\text{ZAMS}} = 12 M_{\odot}$ (J12, J14; Lisakov et al. 2017). For application to subluminous IIP SNe, a $12 M_{\odot}$ model has been shown to produce relatively good agreement with SN 2008bk (Maguire et al. 2012; Lisakov et al. 2017). No spectral calculations exist for the $8\text{--}12 M_{\odot}$ range, a gap in the current theoretical literature we aim to address in this paper. Here, we seek to further advance our knowledge of the lowest mass SNe by modelling late-time spectra. Specifically, the goals of this paper are as follows:

(i) Provide the first nebular-phase (200d–600d) spectroscopic models for Type II SNe from a low-mass ($< 10 M_{\odot}$) progenitor.

(ii) Understand the basic spectral formation processes for such SNe.

(iii) Assess the viability of subluminous Type II SNe to be linked to $8\text{--}11 M_{\odot}$ progenitors by their nebular spectra.

(iv) Analyse whether ECSNe can be spectroscopically distinguished from low-mass Fe CCSNe.

(v) Assess whether any stellar evolution/explosion physics can be constrained from current nebular observations.

(vi) Provide an outlook for things to be learned from future 3D models.

2 MODELLING

We use the SUMO spectral synthesis code (Jerkstrand, Fransson & Kozma 2011; J12) to model the physical state of the ejecta and to compute emergent spectra. SUMO computes the temperature and Non-Local-Thermodynamic-Equilibrium (NLTE) excitation/ionization solutions in each zone of the SN ejecta, taking a large number of physical processes into account. Specifically, the modelling consists of the following computational steps. (i) Emission, transport and deposition of radioactive decay products (gamma-rays, X-rays, leptons). (ii) Determination of the distribution of non-thermal electrons created by the radioactivity (by an expanded Kozma & Fransson 1992, method). (iii) Thermal equilibrium in each compositional zone. (iv) NLTE ionization balance for the 20 most common elements. (v) NLTE excitation balance for about 50 atoms and ions. (vi) Radiative transfer through the ejecta. The solutions are generally coupled to each other and global convergence is achieved by iteration.

The radiative transfer was calculated at a spectral resolution of $\Delta\lambda/\lambda = 3.3 \times 10^{-4}$, corresponding to 100 km s^{-1} , in 4137 frequency bins covering 400–25 000 Å. This guarantees resolution of the most narrow lines from core regions expanding with just a few 100 km s^{-1} .

2.1 Ejecta model

We use the $9.0 M_{\odot}$ progenitor model of Sukhbold et al. (2016). This progenitor is a solar metallicity, non-rotating star, evolved with KEPLER (Weaver, Zimmerman & Woosley 1978) as described in Woosley & Heger (2015) although with a larger network. KEPLER uses efficient semiconvection, which leads to iron core formation down to $M_{\text{ZAMS}} = 9 M_{\odot}$, the lowest mass followed through all burning stages in the grid. The KEPLER calculations employed an adaptive subgrid to follow flame propagations, as well as a large nuclear network of 365 isotopes.

The progenitor is highly degenerate, and ignites Ne, O and Si off-centre in flashes. The Si flash leads to a strong deflagration, otherwise mostly encountered in the $9.8\text{--}10.3 M_{\odot}$ range. The star, with a pre-collapse mass of $8.75 M_{\odot}$, formed an Fe core of $1.32 M_{\odot}$, an O-rich shell of $0.08 M_{\odot}$ and a He shell of $0.17 M_{\odot}$. Outside this was a $7.18 M_{\odot}$ H/He envelope. The composition, density, temperature and Y_e profiles are plotted in Fig. A1 in the Appendix. Some basic properties are listed in Table 1.

2.1.1 Explosion and nucleosynthesis

The progenitor was exploded with two different methods in Sukhbold et al. (2016); with a neutrino simulation using P-HOTB (Janka & Mueller 1996), and with a piston using KEPLER, with properties adjusted to mimic the neutrino simulation. We use as our

Table 1. Properties of ejecta used in the modelling. The masses of selected elements are listed. $M(\text{O})$ (column 5) is the total oxygen mass, and column 6 is the newly synthesized oxygen mass (resides in CO core). Of the original 9 M_\odot , 0.25 M_\odot is lost to stellar winds, and 1.35 M_\odot becomes the neutron star.

Model	M_{ZAMS} (M_\odot)	M_{ejecta} (M_\odot)	E_{kin} (10^{51} erg)	$M(\text{O})$ (M_\odot)	$M(\text{O})$ in CO core (M_\odot)	$M(^{56}\text{Ni})$ (M_\odot)
9	9.0	7.4	0.11	0.072	0.016 (22 per cent)	0.0062

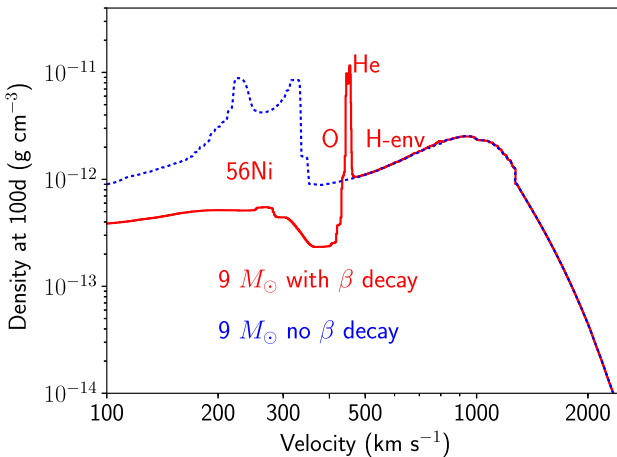


Figure 1. Density profile of ejecta at 100d post-explosion. The standard model with β decay is the red solid line, and the model without decay is blue dotted.

standard case the P-HOTB simulation, which was rerun to include the effects of radioactive decay, as well as to extend to the homologous phase (we run to 100d). We calculate spectra of this model at 200, 300, 400, 500 and 600d. Comparison with the KEPLER model is given in the Appendix. The P-HOTB explosion uses a 4-parameter inner boundary condition to describe the ‘neutrino engine’, where the parameters for the 9 M_\odot model were chosen to reproduce the kinetic energy and ^{56}Ni mass of the Crab nebula when applied to the Z9.6 progenitor model (see Sukhbold *et al.* 2016 for details). These parameters also give good agreement with the main properties of an ab initio 3D simulation (Melson, Janka & Marek 2015).

With this prescription for the explosion, the ejecta obtained a kinetic energy of 0.11 Bethe (1 Bethe = 10^{51} erg) and a ^{56}Ni mass of $6 \times 10^{-3} \text{ M}_\odot$. The homologous density profile at 100d is shown in Fig. 1. The helium core (consisting of the ^{56}Ni , O and He zones) expands with a maximum velocity of 460 km s^{-1} . The radioactive decay has carved out a low-density inner region (the ‘ ^{56}Ni bubble’; Herant & Benz 1992), and pushed the O and He layers from an initial $200\text{--}300 \text{ km s}^{-1}$ into a shell at $430\text{--}460 \text{ km s}^{-1}$. Outside this shell, the envelope density shows an increase to a peak density at about 1000 km s^{-1} followed by a rapid decline.

The P-HOTB explosion models track the composition of H, ^4He , ^{12}C , ^{16}O , ^{20}Ne , ^{24}Mg , ^{28}Si , ^{32}S , ^{36}Ar , ^{40}Ca , ^{44}Ti , ^{48}Cr , ^{52}Fe , ^{56}Ni and tracer nuclei,¹ which we took as stable Fe for mapping into the spectral code (this mass was much smaller than the ^{56}Ni mass). In Section 7 and Appendix B, sensitivity to composition is studied. Inspection of the composition distribution (Fig. 2) shows that the ejecta can be divided into four compositionally rather distinct regions; a ^{56}Ni -dominated inner layer ($0\text{--}425 \text{ km s}^{-1}$), an O-dominated layer

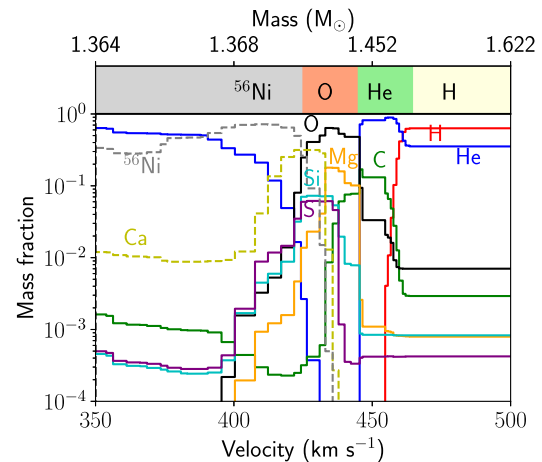


Figure 2. Composition (mass fractions) of the explosion model. The rough division into four compositionally distinct zones is illustrated by the top bar.

($425\text{--}445 \text{ km s}^{-1}$), a He-dominated layer ($445\text{--}465 \text{ km s}^{-1}$) and a H-dominated envelope ($>465 \text{ km s}^{-1}$). For the spectral calculations, the ejecta were divided into shells of 10 km s^{-1} thickness in the He core, and 100 km s^{-1} in the envelope. A higher velocity resolution than 10 km s^{-1} becomes problematic as the code uses the Sobolev approximation, which requires coherence over a Sobolev line width, which is of the order of few km s^{-1} .

Solar composition values for N, Na, Al, K, Sc, Ti, V, Cr, Mn, Co, Ni (species that SUMO can treat but were lacking in the explosion model) were added in the He and H envelopes. Note that signatures for these elements from the deeper layers will be missing in the model.

2.2 Models with dust

There is indication of dust formation in one of the observed candidates we compare the model to (see Section 6.3). Suitable models for this object therefore need to consider dust effects in some manner. Here, we follow earlier methodology (e.g. J12) and apply a uniform absorption coefficient from the centre of the nebula to some maximum velocity V_{dust} . We choose V_{dust} to coincide with the edge of the He core, so $V_{\text{dust}} = 465 \text{ km s}^{-1}$. The amount of dust is chosen by its total radial optical depth τ_d .

3 PHYSICAL CONDITIONS

The physical conditions and processes in the ejecta are now discussed.

3.1 Gamma-ray deposition

Fig. 3 shows the radial gamma-ray optical depth versus time. The low explosion energy makes these SNe dense and gamma-rays are fully trapped for several years ($\tau \gg 1$).

¹ These replace ^{56}Ni as product in reactions in very neutron-rich environment (electron fraction $Y_e < 0.49$).

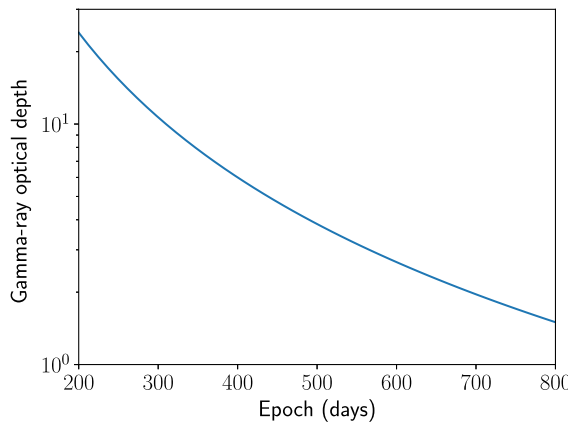


Figure 3. Gamma-ray optical depth as a function of time.

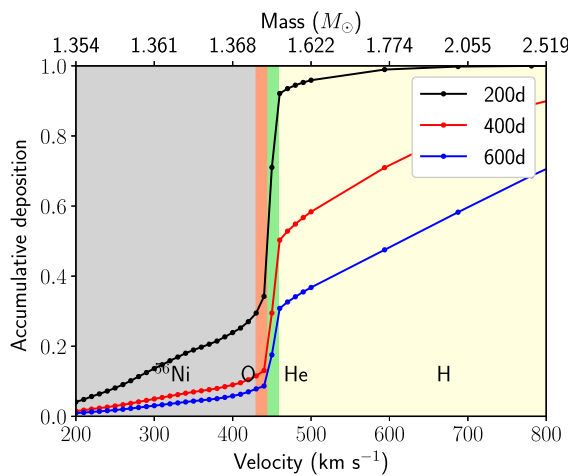


Figure 4. Accumulative energy deposition from radioactive decay products. The zones are labelled with their most abundant element, coloured as grey (^{56}Ni), pink (O), green (He) and yellow (H).

Fig. 4 shows the accumulative gamma-ray deposition as it evolves with time from 200d to 600d. At 200d, the gamma-rays are mostly trapped in the He core, with 30 per cent in the ^{56}Ni layer, 20 per cent in the O layer and 40 per cent in the He layer. Only about 10 per cent penetrate into the H envelope. With time, the fraction reaching the H zone increases though to 50 per cent at 400d and 70 per cent at 600d. Virtually all deposition occurs in the innermost 1000 km s^{-1} at all times, and thus all line profiles should have Half-Width Zero Intensity ($\text{HWZI} < 1000 \text{ km s}^{-1}$).

3.2 Temperature

Fig. 5 shows the temperature evolution. The He core is at $T \sim 5000 \text{ K}$ at 200d, decreasing to $\sim 4000 \text{ K}$ at 400d and $\sim 3000 \text{ K}$ at 600d. At each epoch there is however variation of about 1000 K depending on location. The core is thus relatively hot despite the low ^{56}Ni mass, and one can expect most of the radiative cooling in the optical regime. The inner H envelope is at $T \sim 5000 \text{ K}$ at 200 and 400d, and $\sim 4000 \text{ K}$ at 600d. Note that the temperature peaks around 400d in some parts of the envelope, as the increasing fraction of gamma-ray energy deposited there grows faster with time than the ^{56}Co decline up to around this time.

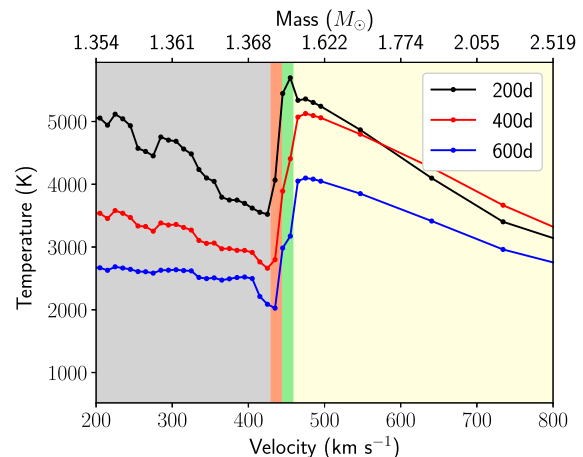


Figure 5. Temperature in the models. The coordinates at zone midpoints are used.

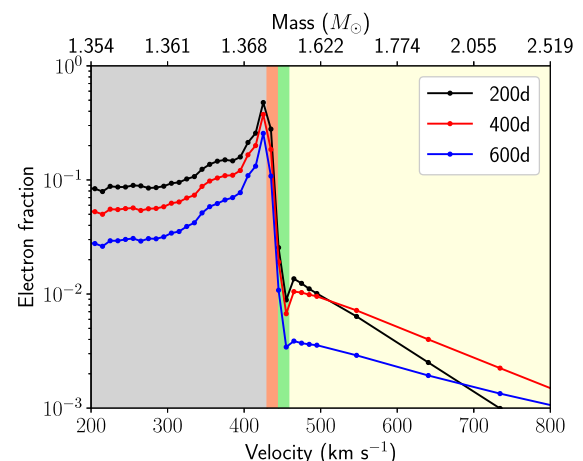


Figure 6. Electron fraction in the models. The coordinates at zone midpoints are used.

3.3 Ionization

The ionization is shown in Fig. 6. The electron fraction $x_e = n_e/n_{\text{nuclei}}$ is around 10 per cent in the inner ^{56}Ni layer, and about 1 per cent in the O/He shells, similar to standard Type IIP models. The lower value in the O/He shells is due to the high-density contrast created by the β decay, and the higher ionization potentials compared to iron-group composition of the ^{56}Ni region. The low gamma deposition in the outer H envelope gives a very low degree of ionization, with x_e falling below 10^{-3} outside 800 km s^{-1} .

Because the electron fraction is low, the spectra will be dominated by neutral and low ionization-potential singly ionized species; thus H I , He I , C I , O I , Mg I , Ca I/Ca II , Si I , S I , Fe I/Fe II can be expected.

3.4 Electron scattering

The electron (Thomson) scattering optical depth at 200d is 0.35, with similar contribution (1/3 each) by ^{56}Ni core, O/He shells and H envelope. Thus, some fraction of emitted photons will experience at least one scattering on their way out. The Thomson scattering creates a mild distortion of line profiles, although this is hardly discernible when convolved with telescope point spread functions since the emitting gas moves so slowly ($\sim 500 \text{ km s}^{-1}$). At 400d

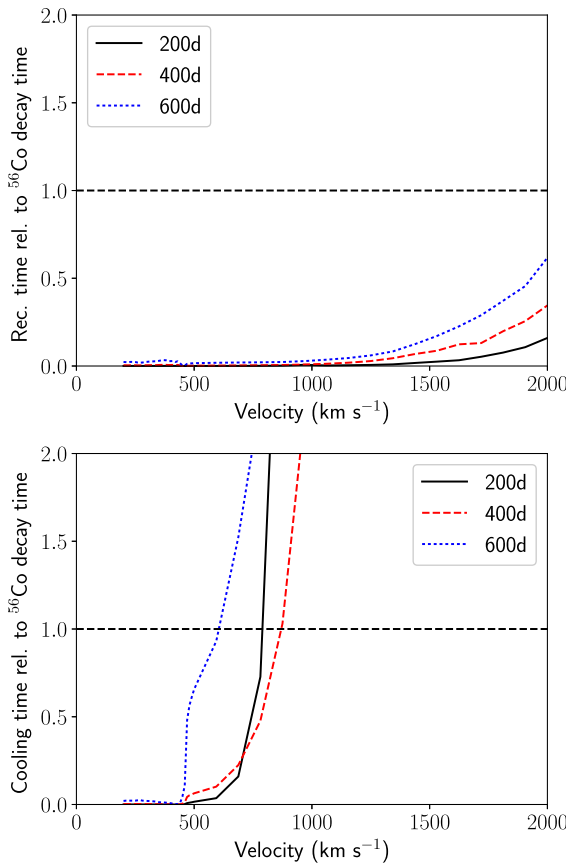


Figure 7. Recombination time-scale (top) and cooling time-scale (bottom) relative to the radioactive decay time-scale.

the Thomson optical depth has dropped to 0.08 and has negligible influence.

3.5 Steady-state verification

SUMO is limited to the assumption of steady state in the ejecta, e.g. that physical processes occur on a shorter time-scale than the dynamic time or the ^{56}Co decay time. In the nebular phase, the ^{56}Co decay time (111d) is the shorter of these. These time-scales can be checked as follows.

3.5.1 Recombination

The recombination time-scale is

$$\tau_{\text{rec}} = \frac{1}{n_e \alpha(T)}, \quad (1)$$

where $\alpha(T)$ is the recombination coefficient. Fig. 7 (top) shows the relative recombination time-scale $\tau_{\text{rec}}/\tau_{^{56}\text{Co}}$, where $\alpha(T)$ for the most common element in the zone was used. Steady state ($\tau_{\text{rec}}/\tau_{^{56}\text{Co}} \ll 1$) is fulfilled for the models at all times.

3.5.2 Cooling

The radiative cooling time-scale is

$$\tau_{\text{cool}} = \frac{\frac{3}{2} n k T}{c(T)}, \quad (2)$$

where n is the total particle density and $c(T)$ is the radiative cooling rate. Fig. 7 (bottom) shows the relative cooling time-scale $\tau_{\text{cool}}/\tau_{^{56}\text{Co}}$. Steady state is fulfilled out to about 500–750 km s $^{-1}$, covering the He core and inner H envelope. This region is responsible for the vast majority of gamma-ray energy reprocessing (Fig. 4), and as such one can expect little difference in a time-dependent model.

4 SPECTRA: THE $9 M_\odot$ MODEL AT 400D

As foundation for the discussion about the spectral formation, we take an in-depth look at the model at 400d. Variations with respect to other epochs will be discussed in Section 5.

The spectrum of this model, together with contributions by various elements, is shown in Fig. 8. Note that in this section the spectra are not convolved to any telescope resolution. To aid in the interpretation, we plot also in Fig. 9 the last interaction zone of the photons as divided into ^{56}Ni core (0–430 km s $^{-1}$), O shell (430–450 km s $^{-1}$), He shell (450–470 km s $^{-1}$) and H envelope (>470 km s $^{-1}$). As composition varies over small velocity intervals that is comparable to the binning, this division is somewhat ‘smeared’, and emission from these specific compositions is not as ‘clean’ as in higher M_{ZAMS} models. For example, some ^{56}Ni emission becomes part of the O-zone emission. A relatively clean Si/S region normally exists, but here the Si/S is always mixed with a larger amount of O.

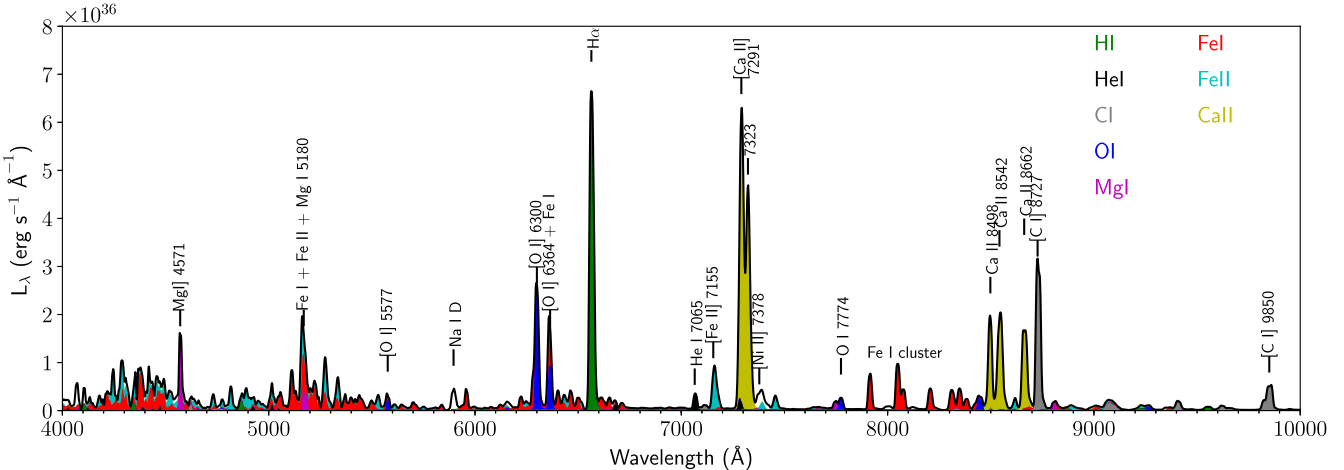


Figure 8. Model spectra of $9 M_\odot$ model at 400d. Contributing elements are colour coded.

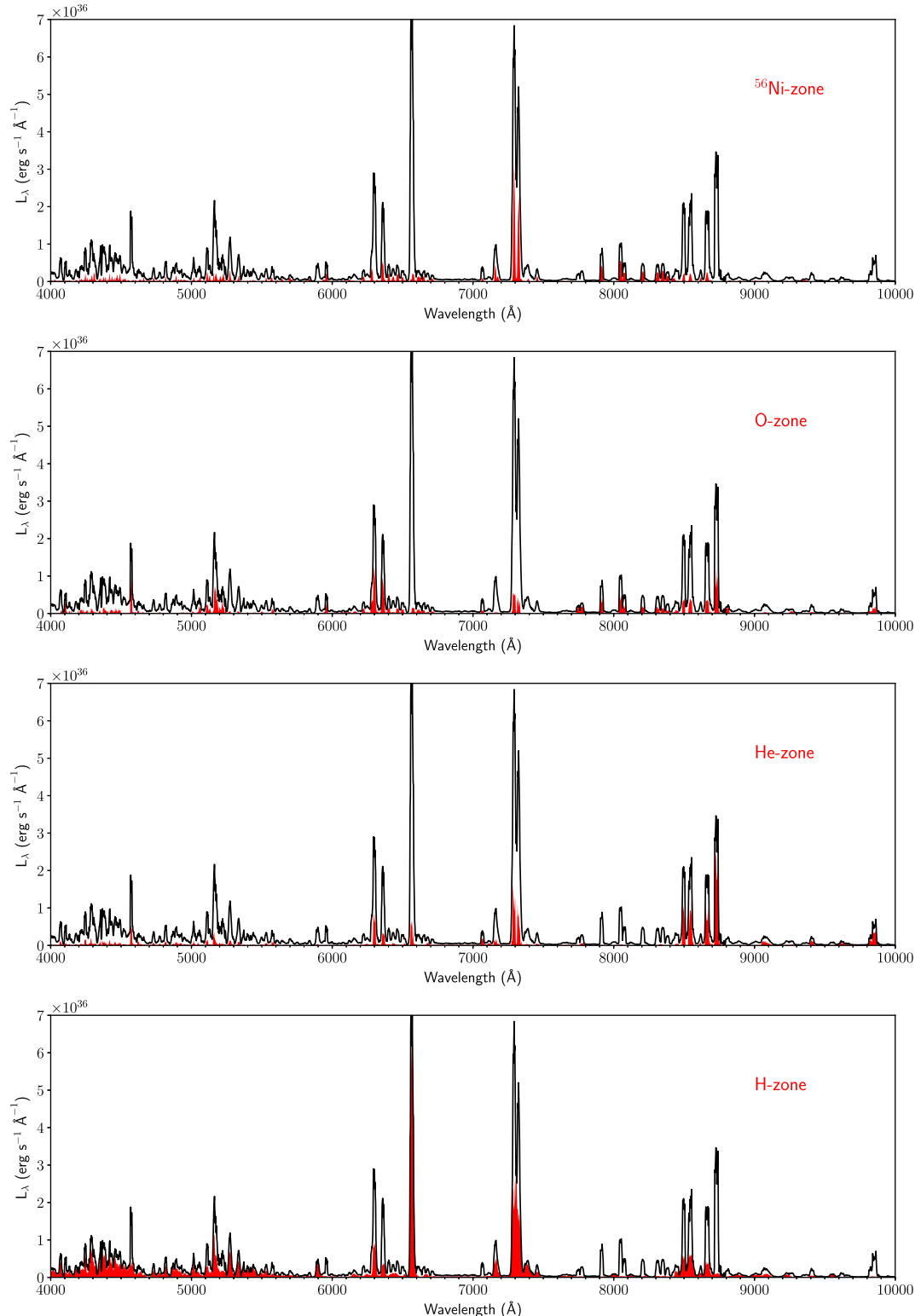


Figure 9. Contribution by different zones to the last interaction of photons, $9 M_{\odot}$ model at 400d. The total spectrum is the black line, and red filled are zone contributions.

As emission comes mainly from the metal core and inner H envelope, line profiles are narrow with FWHM $\lesssim 1000 \text{ km s}^{-1}$. Table 2 shows a summary of FWHM values in the model spectrum. The layered structure of the model is reflected by the increase from

800 km s^{-1} for the iron core lines to 1100 km s^{-1} for H α . Below comments on emission from each species are given.

Hydrogen. Hydrogen displays only one line in the optical; H α . H α emits mainly by recombination. Ionization is dominated by

Table 2. FWHM widths in model at 400d.

Line	FWHM (km s ⁻¹)	Comment
H α	1100	
He I 7065	900	Box-like
[C I] 8727	900	Box-like
[O I] 6300, 6364	900	
Mg I] 4571	900	Box-like
[Ca II] 7291, 7323	900	
[Fe I] 7912	800	Box-like

Balmer photoionization, rather than non-thermal. H α is optically thick out to about 1700 km s⁻¹, and so a clearly seen absorption trough is also produced. The inner ± 500 km s⁻¹ is flat-topped as there is no H in the core.

Helium. Helium displays a weak but distinct He I 7065. This line is produced mainly by the He shell, and thus provides an interesting diagnostic of this layer. However, there is also a contribution ($\sim 1/3$) from freeze-out He in the ^{56}Ni core. Other He lines are too weak to be discernible.

Carbon. Carbon displays [C I] 8727, which is one of the strongest lines in the spectrum, and [C I] 9850, significantly weaker but also unblended. As He I 7065, these lines come from the (C-rich) He zone. The high C abundance here (13 per cent) makes carbon an important cooling agent of this zone (~ 20 per cent of total cooling), which reprocesses ~ 20 per cent of the gamma energy. With a heating fraction of ~ 40 per cent, a total of $0.2 \times 0.4 \times 0.2 = \sim 2$ per cent of the radioactive energy emerges in [C I] 8727. Carbon is mainly neutral (> 90 per cent), which gives robustness for the C I emission. The optical depth is around unity.

This line gives promise to be used both as a signature of these low-mass models, and/or to test the amount of C that exists in the He layer, in turn a diagnostic of He shell burning. There is a distinction here to higher mass CCSN models, where this line is formed mainly in the C/O zone (Jerkstrand et al. 2015b), which is prone to CO molecule formation and ensuing quenching of atomic emission lines. CO formation is quenched in a He-dominated zone (Lepp, Dalgarno & McCray 1990), and the [C I] lines are therefore likely robust predictions. Note that the He/C zone mass is $0.16 M_{\odot}$ in the model, whereas the C/O zone is $< 0.01 M_{\odot}$ (see KEPLER model in the Appendix).

Oxygen. Oxygen displays [O I] 6300, 6364 (although the 6364 Å component is blended with a strong Fe I line at a similar wavelength), and weak but distinct [O I] 5577 and O I 7774 lines. While O I 7774 comes exclusively from the O shell, [O I] 6300, 6364 have also some contribution from the He zone (where the O abundance is 3 per cent) and the H zone. In the O shell, oxygen cooling is at a moderate level (5–10 per cent) as there are relatively high abundances of ^{56}Ni , Ca, Si, S, C that are also efficient coolants. The [O I] lines are here marginally optically thin, $\tau_s = 0.1 - 1$ at 400d.

Magnesium. Magnesium shows Mg I] 4571, coming to a large part from the O shell. Although not the dominant contributor the blend at 5180 Å, Mg I 5180 also emits at significant levels. Mg I provides a few percent cooling of the O shell. Mg I] 4571 is optically thick ($\tau_s \sim 10^3$), and its emission is therefore not strongly sensitive to the specific abundance of magnesium in the zone.

Calcium. Calcium shows [Ca II] 7291, 7323 and the IR triplet (Ca II 8498, 8542, 8662). Both multiplets have contributions from all four regions, linked to the strong cooling capability of calcium even at low abundance. The H envelope provides a broad base with about half the total luminosity. The ^{56}Ni region provides about 20 per cent

with the two components of [Ca II] 7291 and 7323 clearly separated. The O and He shells provide minor (~ 10 per cent of luminosity each), but distinct, contributions as well.

Iron. Iron is prominent throughout the optical spectrum, with Fe I lines providing most of the flux in the ‘quasi-continuum’. Virtually all flux below 6000 Å is due to Fe I lines, as well as a cluster of strong lines between 7900 and 8500 Å. Inspection of the zone origins shows that below 6000 Å most photons had their last emission point in the H envelope. At longer wavelengths this contribution is smaller and emission from the iron core dominates, including the 7900–8500 Å cluster of narrow lines. Coming from the innermost region, the Fe I lines have the smallest FWHM at ~ 800 km s⁻¹.

Fe II produces [Fe II] 7155 as the only distinct line, although a few lines in the blue region are also dominated by Fe II. This line has contributions from several of the zones, especially the H zone, and is therefore not a direct diagnostic of the ^{56}Ni core.

4.1 Signature of the He core

Plotting the last interaction zone of the photon packets (Fig. 9) gives a good first idea about the origin of various lines. However, scattering both in lines and with free electrons partially breaks the link to true emissivity creation by thermal processes. Therefore, complementary model runs where zones are ‘switched off’ or interchanged can help in understanding the spectral formation and identifying signatures of each layer.

Fig. 10 compares the spectra of the $9 M_{\odot}$ model with a model where the composition has been replaced by H-zone material throughout (i.e. a pure H-zone nebula). Thus, this comparison illustrates the sensitivity to the presence of He core materials (^{56}Ni , O and He zones), for the same density profile and energy deposition (held fixed).

The comparison confirms that Mg I] 4571, [O I] 6300, 6364 + Fe I 6364, He I 7065, O I 7774, Fe I 5950, the Fe I cluster at 7900–8500 Å, and [C I] 8727 and [C I] 9850 give signatures of the He core, at least for this epoch of 400d. In particular, the He I 7065, Fe I 7900–8500 Å and [C I] 8727 + 9850 lines provide distinct diagnostics, with almost no emission at all in the pure H nebula. O and Mg lines become stronger in the He core model, but the lines are still there in the H-zone model. Note that synthesized sodium is missing in the model, so the Na I D line in both cases is from primordial sodium.

The O I 8446 (and O I 1.13 μm, not shown) is stronger in the H-zone model. This flux comes from a resonance in primordial O I. Emission in Lyβ at 1025.72 Å is absorbed directly in (primordial) O I 1025.76. Fluorescence into 1.13 μm, 8448 Å and 1602 Å follow with close to 100 per cent efficiency. The main implication is that observation of strong O I 8448 and O I 1.13 μm is not indication of synthesized oxygen. On the contrary, high fluorescence requires emissivity in Lyβ, so rather H-rich gas. The model shows that primordial (solar) abundances of O are sufficient to make a strong line.

5 TIME EVOLUTION

Fig. 11 compares the spectra of model 9 at 200d, 400d and 600d. Here, renormalization in flux levels has been done to emphasize changes in spectral shape, so the 200d model is multiplied with $\exp(-200/111)$ and the 600d model with $\exp(+200/111)$, to synchronize powering levels to 400d.

At 200d the spectrum is relatively featureless, with emission lines not yet particularly distinct. Mg I] 4571, [O I] 6300, [Ca II] 7291, 7323 and [C I] 8727, [C I] 9850 have yet to distinctly emerge.

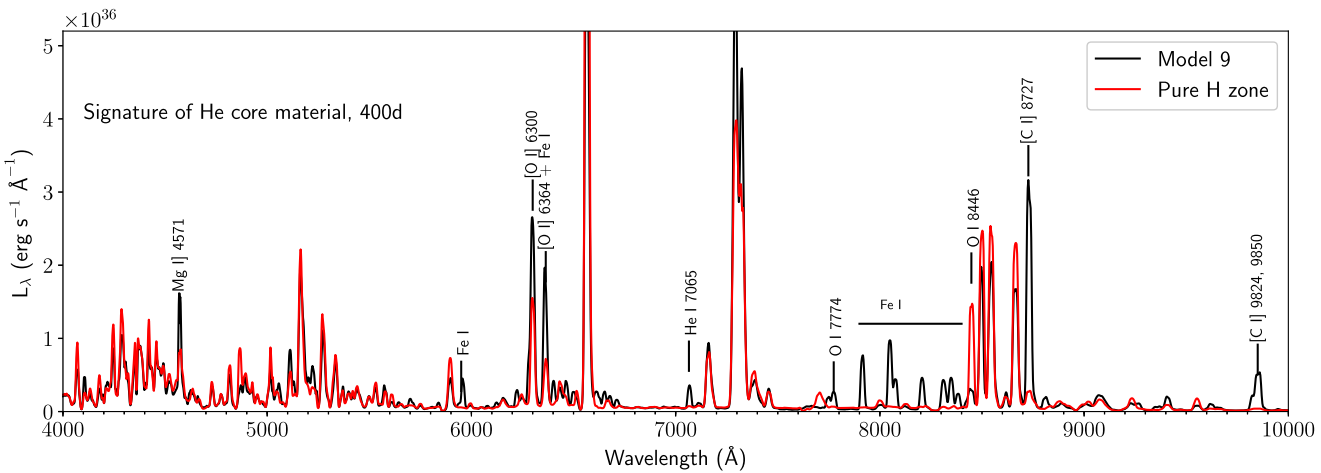


Figure 10. Signature of He core, as illustrated by comparing the standard $9 M_{\odot}$ model (black) with a model where all composition is that of H-zone material (red), at 400d. The main lines differing are labelled.

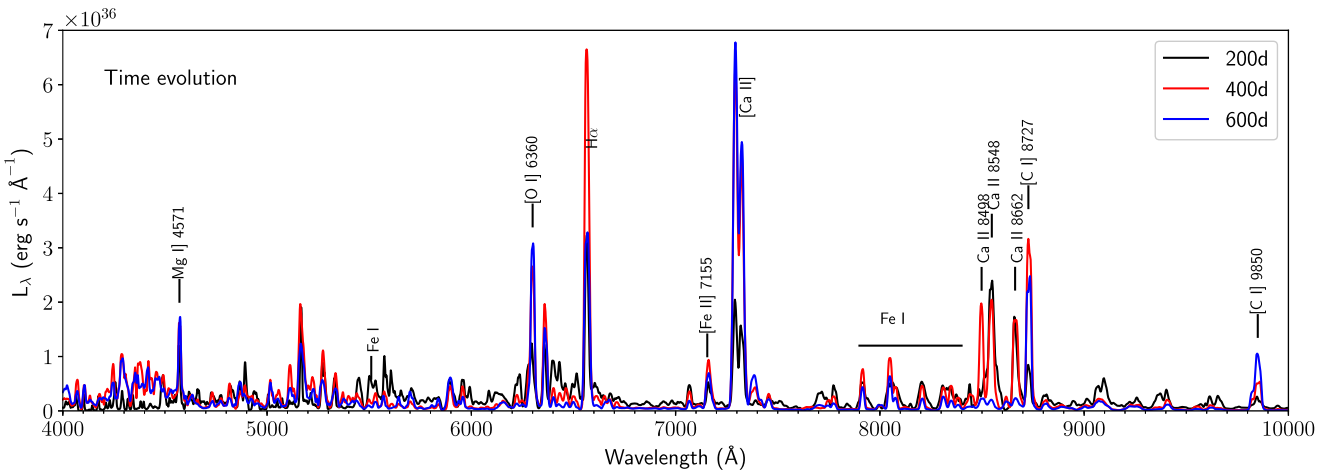


Figure 11. Comparison of the $9 M_{\odot}$ model at 200d (black), 400d (red) and 600d (blue). The 200d model has been scaled down by $\exp(-200/111)$ and the 600d model has been scaled up by $\exp(200/111)$, to normalize all flux levels to 400d.

Fe I and Ca II almost exclusively make up for the optical lines. As discussed in Section 3.1, at 200d a significant fraction of gamma-rays (30 per cent) are absorbed by the ^{56}Ni layer. This makes the Fe I cluster at 7900–8500 Å particularly distinct at this epoch, one of few signatures of the core structure of the SN at this epoch.

Of the bolometric luminosity of $1.45 \times 10^{40} \text{ erg s}^{-1}$, <1 per cent is in the UV ($<3000 \text{ \AA}$), 68 per cent is in the optical (3000–10 000 Å), 25 per cent is in the NIR (10 000–25 000 Å) and 7 per cent in MIR.

At 400d, Mg I 4571, [O I] 6300, 6364, [Ca II] 7291, 7323, Ca II 8498, and [C II] 8727 and [C II] 9850 all ‘breaking out’ far above the quasi-continuum. Most of these lines show a relatively uniform growth between 200 and 400d. The UV, optical, NIR and MIR fractions are now 1.4 per cent, 78 per cent, 13 per cent and 7 per cent, respectively. Note that the UV and optical fractions have increased, as reduced line opacity allows more escape of photons at these wavelengths.

Relatively little evolution is seen between 400d and 600d. H α has reduced its prominence, the Fe I cluster at 7900–8500 Å is now less distinct, and the Ca II NIR triplet has become very weak. The UV, optical, NIR and MIR fractions are now 9.4 per cent, 71 per cent, 11 per cent and 9 per cent, respectively.

In summary, the spectrum is predicted to gradually switch on to a nebular characteristic sometime between 200d and 400d, with Mg I 4571, [O I] 6300, 6364, [Ca II] 7291, 7323, Fe I 7900–8500 and [C II] 8727 all becoming very distinct. Some of these activations are due to delayed gamma-ray penetration into the He and H layers (e.g. for [C II] 8727) whereas some are more due to changing physical conditions and reduced optical depths.

6 COMPARISON WITH OBSERVATIONAL CANDIDATES

Three low-velocity Type II SNe have nebular spectra published; SN 1997D (Turatto et al. 1998; Benetti et al. 2001), SN 2005cs (Pastorello et al. 2009) and SN 2008bk (Maguire et al. 2012). Here, we compare our models in turn to these three.

6.1 SN 1997D

SN 1997D was discovered on 1997 January 14 (MJD 50462) in NGC 1536 by de Mello, Benetti & Massone (1997). It was then already at the end of the plateau phase, so the explosion epoch is ill constrained.

No distinct Na I D could be seen (Turatto et al. 1998), and we use only the galactic extinction component $E(B - V) = 0.02$ mag (Zampieri et al. 2003) here. NGC 1536 has only a single distance measurement in NED,² at 13.4 Mpc (Tully 1988), which we use. We assume a recession velocity of 1217 km s^{-1} (NED). Regarding ^{56}Ni mass, Turatto et al. (1998) and Benetti et al. (2001) estimate $2 \times 10^{-3} M_{\odot}$ by comparing optical photometry to SN 1987A, with what appears to be an assumed discovery age of 50d. This is a factor 3 lower than in our model, and we therefore expect to have to scale all spectra by a factor $\sim 1/3$ to reach flux agreement. This is larger than desired, but we demonstrate in the Appendix by comparing P-HOTB and KEPLER models that lowering by the ^{56}Ni mass by a factor 2 has only limited impact. We note, however, that Zampieri et al. (2003) inferred $8 \times 10^{-3} M_{\odot}$ with an assumed discovery age of 100d.

Nebular data set. Three nebular-phase spectra were presented in Benetti et al. (2001), on 1997-05-01 (MJD 50569), 1997-09-21 (MJD 50712) and 1998-02-02 (MJD 50846). Assuming an explosion epoch of 100d before discovery (MJD 50362), giving a typical plateau length of 110d, this implies epochs of +207d, +350d and +484d. The spectral resolution varied between 7 and 17 Å over the data sets and the wavelengths. Taking 12 Å at 6000 Å as representative numbers, the resolution is about 600 km s^{-1} .

The +207d and +350d spectra show reasonable agreement with contemporary photometry in Benetti et al. (2001). The +484d spectrum is, however, a factor 4.5 brighter than the contemporary V -band photometry, presumably due to some issue with the flux calibration. The spectrum was therefore scaled down by a factor of 4.5. This produced consistency in the amount of rescaling needed for the model comparisons.

Fig. 12 shows comparisons of the three nebular spectra with the $9 M_{\odot}$ model. Here, the model has been convolved with a Gaussian with $\text{FWHM} = 600 \text{ km s}^{-1}$ to match the telescope resolution.

6.1.1 +207d

At 207d a model scaling of $X = 0.61$ is required to match the overall optical luminosity, which corresponds to a ^{56}Ni mass of $3.8 \times 10^{-3} M_{\odot}$. The colour agreement between model and data is reasonably good, although the model is somewhat bluer. There are also reasonably matching line profiles and luminosities for H α , [Ca II] 7291, 7323 and Ca II 8548, 8662. Note how Ca II 8498 is suppressed both in the model and in the SN. The 1:1 ratio of [Ca II] 7291 and 7323 means the lines are still optically thick.

The observed spectrum is noisy beyond 7500 Å, and there are not many more clearly identified emission lines. At this epoch [O I] and Mg I] lines have not clearly emerged yet, either in the model or in the observed spectrum. In the blue region, $\lesssim 5500$ Å, there is somewhat too much ‘fine-structure’ in the model, with too many strong narrow lines. The model makes two strong iron lines at 5180 and 6364 Å that are not observed.

6.1.2 +350d

At 350d, a scaling $X = 0.45$ is required (^{56}Ni mass $2.8 \times 10^{-3} M_{\odot}$). Mg I] 4571 and [O I] 6300, 6364 have now emerged and the model predictions match the observed spectrum well. Detection of He I 7065 is now clearly confirmed (marginally seen at 207d). All these

lines clarify the presence of He core material. Also [Ni II] 7378 is distinct in this observed spectrum.

Fig. 13 shows zoom-ins of selected strong lines at this epoch. H α fits well, just slightly too broad in the model. The flat-top has been washed out by the 600 km s^{-1} convolution, and a rounded peak is seen also in the data. The emitting region is clearly bounded at about 1000 km s^{-1} , which supports the model calculation that gamma-rays cannot penetrate further.

He I 7065 shows good agreement. From the observed line profile the He emitting region is smaller, $V \lesssim 600 \text{ km s}^{-1}$, supporting the stratified structure with the He shell interior to the H envelope.

While the red wing of [O I] 6300 shows agreement, there is contamination in the model by an Fe I line on the blue side that is not observed.

The [Ca II] lines are about 25 per cent too broad in the model. The contribution at high velocities in the model is due to the inner H envelope, but such a component is not seen in the data. This is a difficult discrepancy to resolve since [Ca II] is normally an important cooler of H gas.

Finally, the observed [Fe II] 7155 line has formally a lower FWHM (730 km s^{-1}) than the previously discussed lines, which supports a significant contribution by synthesized iron in a region interior to O, He and H layers.

Table 3 summarizes the observed FWHM and comparison with the model ones. Here, the ‘deconvolved’ FWHM is obtained from $\text{FWHM}_{\text{obs}}^2 = \text{FWHM}_{\text{dec}}^2 + \text{FWHM}_{\text{teles.}}^2$, which holds if both intrinsic line and instrument PSF are Gaussians. Overall the model gives somewhat too broad lines.

6.1.3 +484d

At 484d there is continued matching to Mg I and [O I] lines. There is no strong change in the rescaling required ($X = 0.71$), which means that there is no indication of dust formation or gamma-ray escape yet. Note that the [Ni II] 7378 line is made by primordial nickel in the model. One discrepancy is that, whereas the observed [O I] 6300-to-6364 ratio is now approaching the optically thin 3:1 ratio, the model ratio is still close to 1:1 due to Fe I line contamination. While a factor ~ 2 too high ^{56}Ni mass in the model is one factor in this overproduction, there likely remain other discrepancies that make too strong Fe I lines in the model.

6.1.4 Discussion

Overall, this $9 M_{\odot}$ model, with no tuned parameters at all to fit the data, provides a convincing spectral fit to SN 1997D, which strengthens the hypothesis of an origin as a low-mass star. Both line luminosities and line profiles are in good agreement with the model. The estimated FWHM in Table 3 implies an emitting region $\sim 400\text{--}800 \text{ km s}^{-1}$, close to the size of the gamma-trapping region in the model.

Although there are no observations of the spectral region containing carbon lines, He core material is convincingly established by the presence of He I 7065, Mg I] 4571 and [O I] 6300, 6364, with the right expected luminosities. The presence of these lines suggests that SN 1997D was an Fe CCSN, not an ECSN.

Taking the average scaling factor X we need to match the model flux level to each observed spectrum, our estimate for the ^{56}Ni mass in SN 1997D becomes $3.6 \times 10^{-3} M_{\odot}$. The model, with $6.2 \times 10^{-3} M_{\odot}$, gives slightly too broad lines, which is consistent

² <https://ned.ipac.caltech.edu>

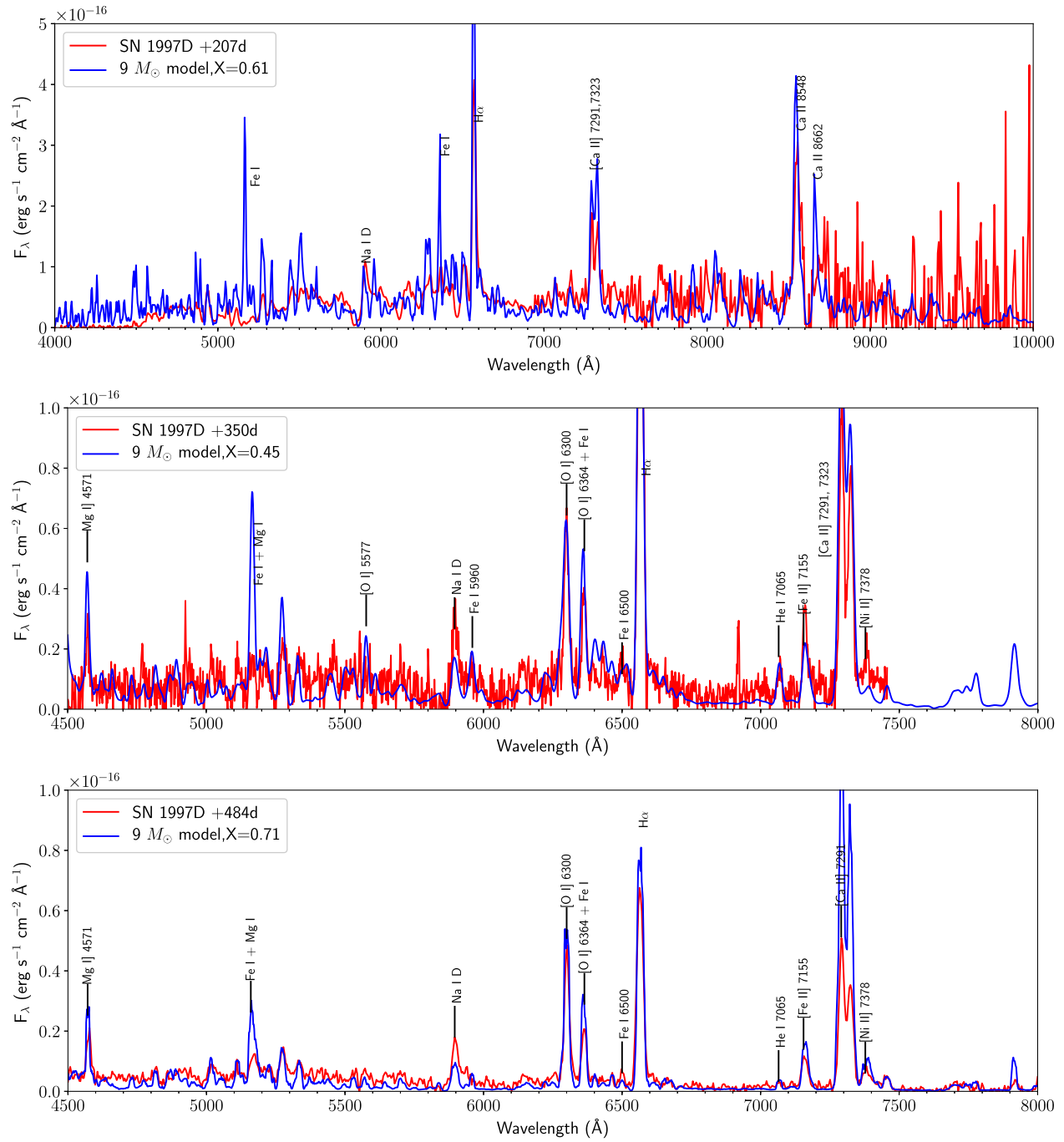


Figure 12. Top: SN 1997D at +207d (red) compared to the $9 M_{\odot}$ model (blue), at 200d rescaled with $\exp(-7/111)$ and a factor $X = 0.61$ (to compensate for the lower ^{56}Ni mass). Middle: SN 1997D at +350d (red) compared to the $9 M_{\odot}$ model (blue), at 300d rescaled with $\exp(-50/111)$ and $X = 0.45$. Bottom: SN 1997D at +484d (red) compared to the $9 M_{\odot}$ model (blue), at 500d rescaled with $\exp(+16/111)$ and $X = 0.71$. The model spectra have been convolved with a Gaussian with $\text{FWHM} = 600 \text{ km s}^{-1}$ to match the telescope resolution.

with a higher ^{56}Ni mass than observed, as this is linked to a higher explosion energy.

6.2 SN 2005cs

SN 2005cs was discovered on 2005 June 28 (MJD 53549) by Kloehr et al. (2005) in the Whirlpool galaxy (M51), with pre-explosion limits of about 1 d earlier (Pastorello et al. 2006). We take the explosion epoch as 2005 June 27 (MJD 53548).

Nebular data set. Pastorello et al. (2009) present nebular spectra at intervals of ~ 2 months up to +333d, all available on WiseRep (Yaron & Gal-Yam 2012).³ To resolve the intrinsic narrow-line structure of these low-velocity SNe, it is beneficial to use the highest resolution spectra taken. These ($\text{FWHM} \sim 300 \text{ km s}^{-1}$) correspond to the observations on 2006-01-07 (+194d), 2006-03-25 (+270d),

³ <http://wiserep.weizmann.ac.il>

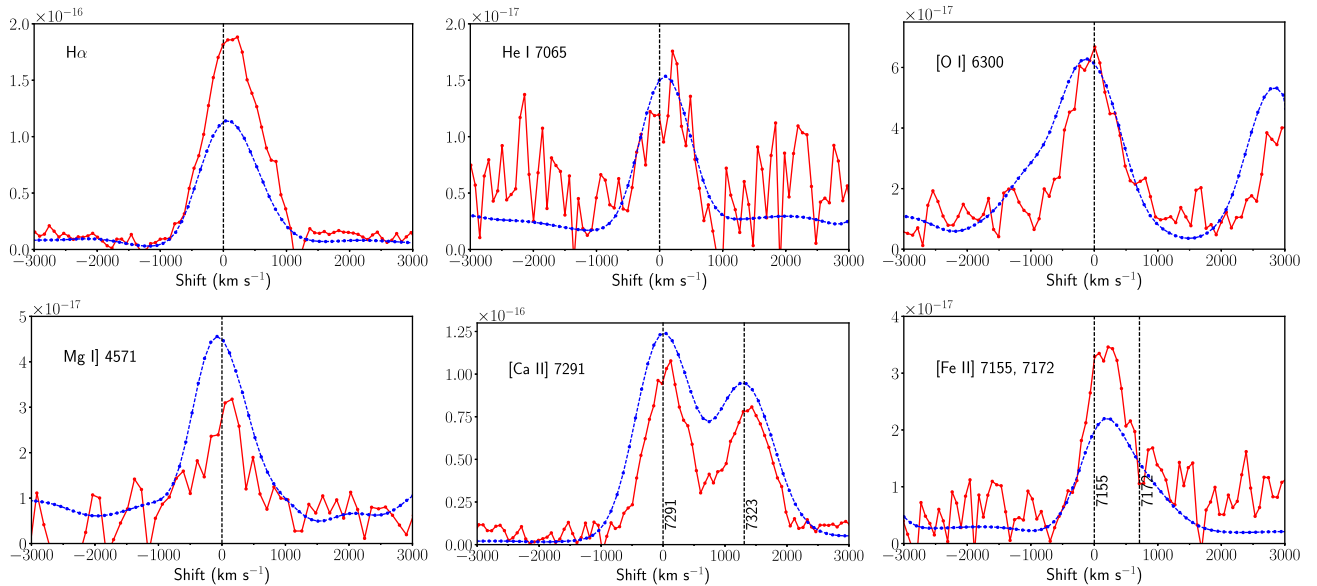


Figure 13. Zoom-in on-line profiles at +350d in SN 1997D (red, solid) and in the $9 M_{\odot}$ model (blue, dashed). The model spectrum has been convolved to the telescope resolution of 600 km s^{-1} .

Table 3. Observed line profile widths in SN 1997D, at +350d, compared to the model (unconvolved) values.

Line	FWHM _{obs.} (km s ⁻¹)	FWHM _{dec.} (km s ⁻¹)	Model (km s ⁻¹)
H α	1020	820	1100
He 7065	950	740	900
[O I] 6300, 6360	940	720	900
[Ca II] 7291	820	560	900
[Fe II] 7155	730	420	800

2006-04-01 (+277d) and 2006-04-05 (+281d). The similar epochs of the last three make it sufficient to study one, which we choose as day +277. The spectra at +226d and +333d are at lower resolution. A NIR spectrum exists at +281d, which we also study. We convolve the model spectra with matching Gaussians of FWHM = 300 km s^{-1} for the comparisons.

The raw nebular spectra are heavily contaminated by background light (Pastorello, private communication). The extraction therefore involved the subtraction of a blackbody that was fit to the estimated photometry of the contaminating light (from difference in synthetic photometry on total spectra and template-subtracted photometry of the SN). The combination of a large contrast between background/SN light and lack of a template spectrum of the region means that there is significant uncertainty in the resulting SN spectrum. For example, at +277d the contamination is 90–95 per cent of the flux in the blue and ~ 70 per cent in the red (Pastorello, private communication). While errors due to continuum subtraction are moderate in the red, in the blue the uncertainty is much larger. For example, a 5 per cent error in the continuum estimate (say from 90 to 95 per cent) results in a factor 2 error in the SN residual (from 5 to 10 per cent). The consequence is that we have to treat the spectral data in the blue with caution but can trust it more in the red. Agreement between synthetic photometry on the spectrum and template-subtracted photometry is generally good, but slit losses or flux calibration errors cannot be checked with this method, and any such loss would be compensated by added background light. Focus

for model comparison should therefore be on line luminosities, to factor ~ 2 , but less on spectral shape, particularly in the blue.

Fig. 12 in the Appendix compares the first SN 2005cs spectrum at +194d to SN 1997D at a similar epoch. While SN 1997D also has a declining blue tail, it is less dramatic, and the overall spectrum is bluer. There is also more fine structure in the blue in SN 1997D. Fig. 7 in Pastorello et al. (2009) shows that subluminous IIP SNe differ colour-wise to normal IIP SNe mainly in the early tail phase (120–200d), where they are 0.5–1 mag redder in $B - V$ and $V - R$. SN 2005cs is the most extreme case in $V - R$, while SN 1997D has similar values for $B - V$. The spectrum does have the correct $V - R$ value.

Extinction. Maund, Smartt & Danziger (2005) estimated $E(B - V) = 0.16$ mag from Na I D lines, and $E(B - V) = 0.12$ mag from analysis of surrounding red supergiants. Other authors have found similar values $E(B - V) = 0.05 - 0.2$ mag from the Na I D lines (Li et al. 2006; Pastorello et al. 2006). Baron, Branch & Hauschildt (2007) found $E(B - V) = 0.035 - 0.05$ mag from spectral modelling, and Brown et al. (2007) and Dessart et al. (2008) had similar results. A reasonable choice to use is the average value of these estimates, $E(B - V) \sim 0.1$ mag, which we use here. All three methods consistently give $E(B - V) < 0.2$ mag, which robustly tells us that the extinction is small/moderate and does not introduce any major uncertainty.

Distance and recession velocity. We use the median NED distance of 8.1 Mpc (standard deviation 1.2 Mpc). The distance has been estimated by PNLF, SBF, TRGB, EPM, SEAM, and Tully–Fisher methods with relatively consistent results. Apart from SN 2005cs, also SN 1994I and SN 2011dh exploded in this galaxy, giving multiple occasions to use the EPM and SEAM methods. Finally, we Doppler correct the spectra with 600 km s^{-1} (NED).

It should be mentioned here that the estimated bolometric luminosity of the SN declined slower than ^{56}Co decay (Pastorello et al. 2009) in the tail phase, thus making it unclear whether residual energy from the explosion or other energy sources were important at late times. We do not attempt to consider any other sources here, but mention this caveat/uncertainty. Utrobin, Chugai & Pastorello (2007) find from models a possible explanation to be

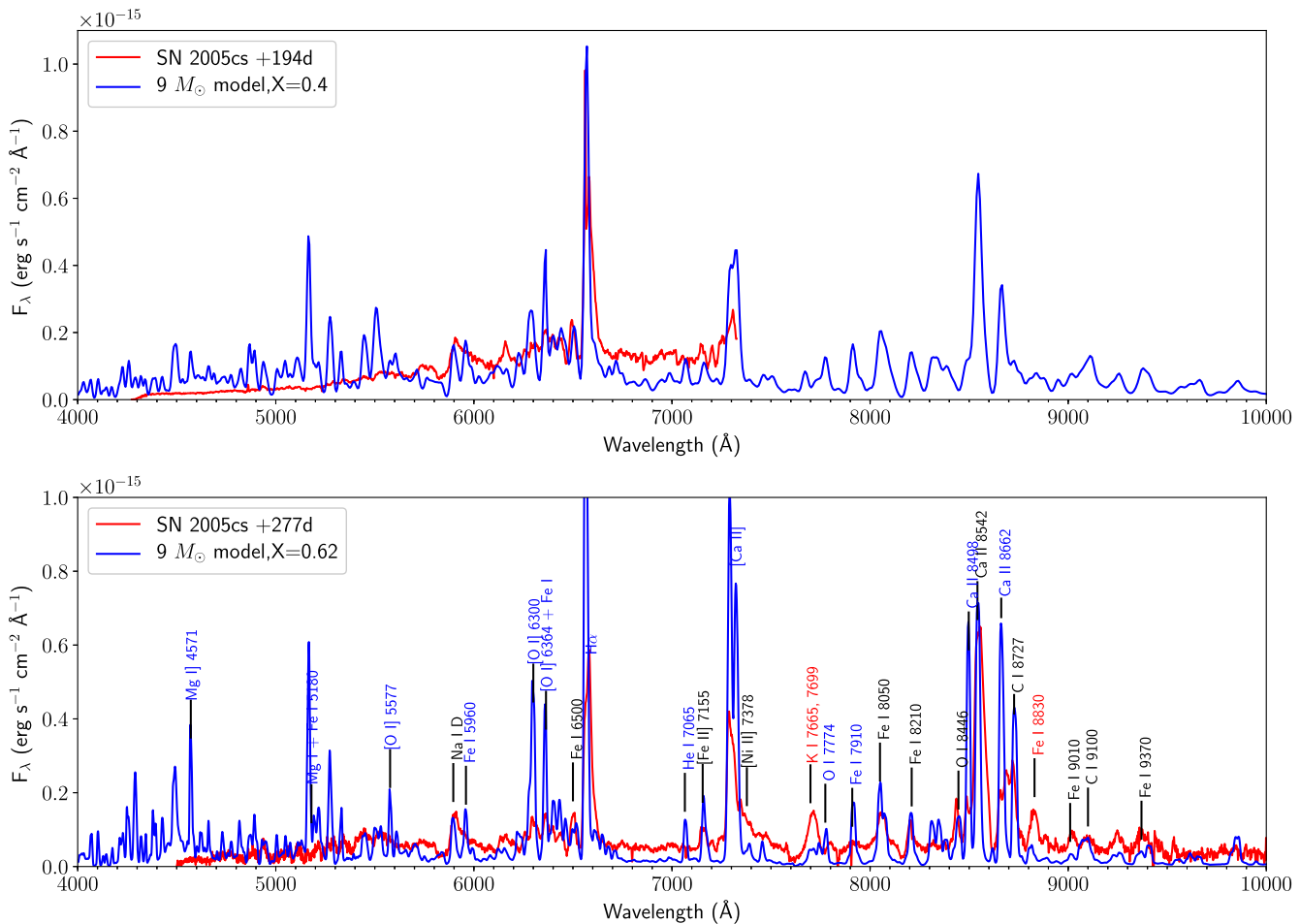


Figure 14. Top: SN 2005cs at +194d (red) compared to the $9 M_{\odot}$ model (blue), at 200d rescaled with $\exp(6/111)$ and $X = 0.4$. Bottom: SN 2005cs at +277d (red) compared to the $9 M_{\odot}$ model (blue), at 300d rescaled with $\exp(23/111)$ and $X = 0.62$. The model spectra have been convolved with a Gaussian with $\text{FWHM} = 300 \text{ km s}^{-1}$ to match the telescope resolution. Well-reproduced lines are labelled in black text, overproduced in blue and underproduced in red.

residual energy from the shock passage still leaking out in the early tail phase, although in the models these effects last for a few weeks rather than a few months as observed in SN 2005cs. After 330d, the observed decline rate steepened somewhat, perhaps going on to a true ^{56}Co tail (Pastorello et al. 2009), although with only two observed epochs between 330 and 400d, it is hard to tell, and the bright background also introduces significant uncertainties even in template-subtraction approaches.

This deviation from a ^{56}Co decline rate makes it unclear even if there is any ^{56}Ni in SN 2005cs. One cannot a priori rule out that the late-time luminosity is generated by circumstellar interaction, for instance. This issue makes it important to see whether we can identify any lines unambiguously coming from a ^{56}Ni region in the SN.

6.2.1 +194d

Fig. 14 (top) compares SN 2005cs at +194d with the $9 M_{\odot}$ model at 200d. A model scaling of $X = 0.4$ was used to reach overall flux agreement, which would correspond to a ^{56}Ni mass of $2.4 \times 10^{-3} M_{\odot}$. This is close to the mass estimated by Pastorello et al. (2009) by comparison of the bolometric luminosity with SN 1987A ($3 \times 10^{-3} M_{\odot}$).

But the spectral agreement is poor. The observed spectrum still appears photospheric in character, with few distinct emission lines apart from $\text{H}\alpha$. It is almost completely featureless below 5700 Å, although as stated above the blue region involves significant calibration uncertainty. The model, on the other hand, produces many narrow lines in the blue. This tendency was present also for SN 1997D at 200d, although not as extreme as here. We note that the factor 2 lower ^{56}Ni mass needed for SN 2005cs compared to the model would correspond to a lower explosion energy and yet lower velocities, which would (probably) worsen the problem of too narrow lines in the model.

The structure of the model at this epoch is a highly powered He core (expanding with $\sim 450 \text{ km s}^{-1}$), absorbing 90 per cent of the gamma-rays. Powering appears to occur at higher velocities in SN 2005cs, but this would involve obtaining a lower ^{56}Ni mass at a higher explosion energy. Another, and perhaps more plausible situation, is that there is more mixing in this SN.

6.2.2 +277d

At +277d the observed spectrum shows somewhat more prominent emission lines and fine-structure (Fig. 14, bottom panel), and general agreement with the model is somewhat improved. The model

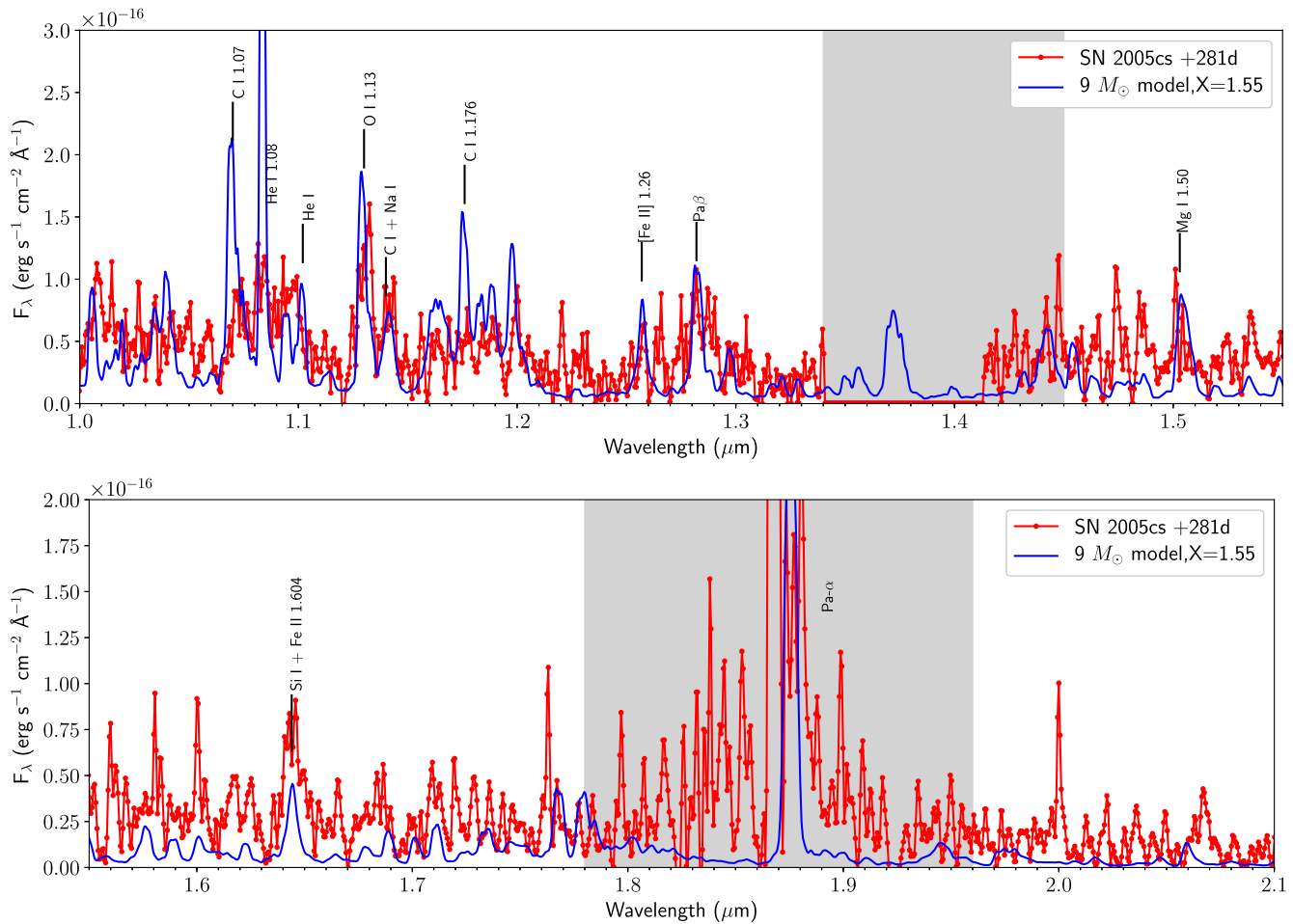


Figure 15. SN 2005cs at +281 in the NIR (red) compared to the $9 M_{\odot}$ model (blue). The model spectra have been convolved with a Gaussian with FWHM = 300 km s^{-1} to match the telescope resolution. Gray regions mark telluric bands.

has still, however a too high ratio of narrow emission lines to ‘quasi-continuum’.

Fig. 15 shows the NIR spectrum compared to the same model. The model requires an upscaling of $X = 1.55$. The observed spectrum is of low S/N, and there are few certain line detections. O I 1.13 μm and [Fe II] + [Si I] 1.64 μm seem robustly detected. A few more look like plausible detections (He I + S I 1.08 μm , Na I 1.14 μm , Si I 1.20 μm , [Fe II] 1.26 μm , Pa β 1.28 μm , ?1.47 μm , Mg I 1.50 μm , ?1.58 μm , Br δ 1.79 μm and ?2.0 μm), where question marks denote unknown line matches. There are potentially many more real lines, but what is noise and what is a line is hard to tell.

The observed optical spectrum shows strong, broad Na I 5890, 5896 and K I 7665, 7699 scattering lines. The blue absorption edges of these extend to about 3000 km s^{-1} , with the red emission reaching $2000\text{--}3500 \text{ km s}^{-1}$ for Na I and 2000 km s^{-1} for K I. The model envelope ends at 2000 km s^{-1} and thus does not fully capture these lines. These lines arise by scattering by primordial Na and K in the H envelope, which must have a density at 3000 km s^{-1} high enough to make these lines optically thick.

Some predicted lines of Fe, Ca and C can now be clearly identified in the observed spectrum: [Fe II] 7155, [Ca II] 7291, 7323, Fe I 8047, Fe I 8204, Ca II NIR, [C I] 8727, Fe I 8830, Fe I 9010 and Fe I 9370. The presence of Fe I lines in the observed spectrum is quite convincingly established, in particular through the strong Fe I 8047, 8075. However, as at 200d the model puts out stronger blue lines

(e.g. Mg I] 4571, Mg I + Fe I 5180, [O I] 6300, 6364) than observed. Some more detailed comments on emission lines from the major species are given below.

Hydrogen. The model produces mainly H α , a factor several too bright (the peak flux is $1.6 \times 10^{-16} \text{ erg s}^{-1} \text{ cm}^{-2} \text{ \AA}^{-1}$). The observed line (Fig. 16) is broad (FWHM = 2000 km s^{-1}), quite flat-topped and strongly asymmetric with emission on the blue side extending to 800 km s^{-1} , but to 2500 km s^{-1} on the red side. The model line is too narrow (FWHM = 1100 km s^{-1}), as mainly the inner part of the H envelope absorbs the gamma-rays (Fig. 4). This suggests that the model core is too dense.

Helium. He I 7065 is strong in the model but, in contrast to SN 1997D, is not observed in SN 2005cs. Similarly, in the NIR He I 1.08 is strongly overproduced (Fig. 15). Thus, there is no clear sign of He in the observations. It is tempting to draw a conclusion that there is no He shell present. However, carbon lines from this zone appear to be seen (more below).

Carbon. [C I] 8727 appears to be observed in reasonable correspondence with the model, although it is blended with another (unidentified) line on the blue side. Of the two other reasonably strong C I lines predicted, C I 9100 also appears to be seen (although at low contrast), but [C I] 9850 not, however the last line lies at the noisy end of the spectrum. In the NIR, the model overproduces C I 1.07 and 1.176 μm , completing an overall picture that the model somewhat overproduces C lines.

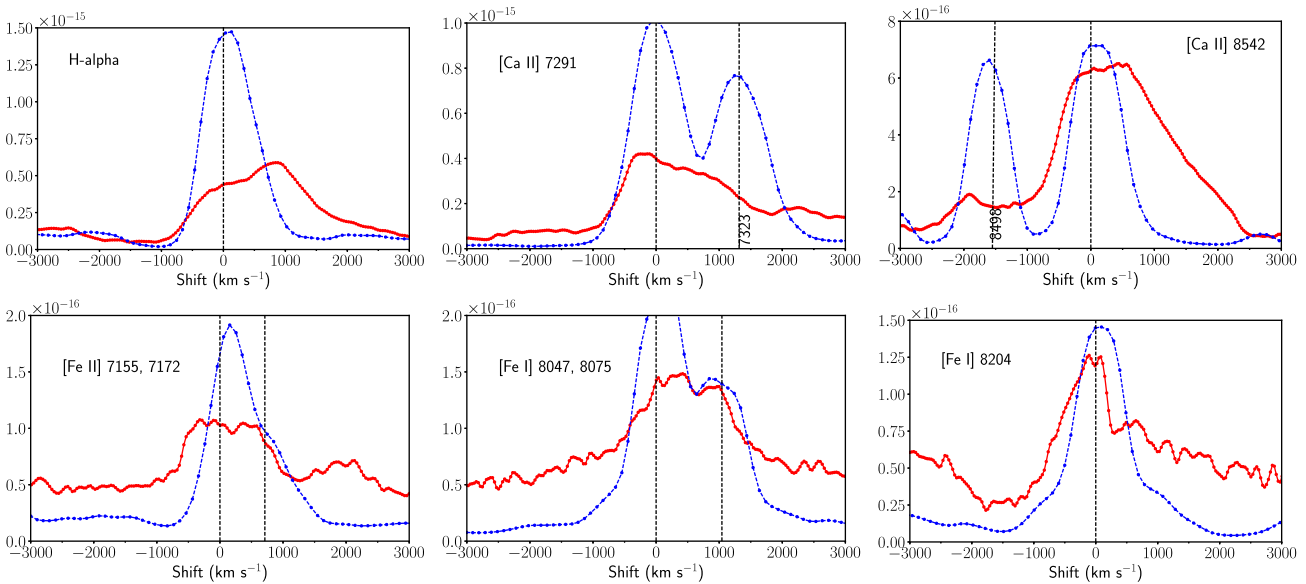


Figure 16. Observed (red, solid) and modelled (blue, dashed) lines in SN 2005cs.

Oxygen. There is no sign of O I 7774, which is distinct in the model. Regarding $[\text{O I}]$ 6300, 6364, there are two observed bumps, exactly peaked at 6300 and 6364 Å, that likely are due to $[\text{O I}]$ 6300, 6364. They have FWHM of 1500 km s^{-1} ($[\text{O I}]$ 6300) and 1000 km s^{-1} ($[\text{O I}]$ 6364), likely differing somewhat due to blending effects. The model makes much too strong $[\text{O I}]$ lines, of which there is also significant Fe I contribution (~ 50 per cent) at 300d (6280 and 6360 Å). At 300d, there are contributions from all zones to this feature, although mainly from the O/He shell. The model also predicts a distinct $[\text{O I}]$ 5577 that is not observed. Thus, overall the model strongly overproduces emission from the O shell. The O I 8446 line is observed and reasonably well matched by the model, but this line is from the H zone.

Magnesium. The model predicts a distinct Mg I 4571 that is not observed, although the spectral coverage ends exactly around this wavelength. The strong model line at 5180 Å (also unobserved) has also a Mg contribution. Overproduction of Mg lines is consistent with the overproduction of O lines, as these arise from similar regions. There is no detection of Mg I 4571 in any earlier nebular spectra of SN 2005cs that had extension further in the blue (fig. 13 in Pastorello et al. 2009, note the region was not observed in the last epoch of 333d), which is dim and featureless in the blue throughout the nebular phase. The reason may be that with the bright blue background and low ^{56}Ni mass, the SN had faded below detection limit.

The model also predicts a strong Mg I 1.50 μm (somewhat blended with Fe I 1.51 μm), but neither of this is a clear detection (Fig. 15).

Silicon. The model produces no optical lines, and none is observed. The model produces 1.20 μm and 1.64 μm emission, but these are swamped by iron line emission. Thus synthesized silicon cannot be diagnosed.

Ca doublet. The $[\text{Ca II}]$ 7291, 7323 line has an odd observed shape (Fig. 16). The blue wing of $[\text{Ca II}]$ 7291 indicates a maximal expansion of about 800 km s^{-1} , similar to $\text{H}\alpha$. A peak is seen just blueward of 7291 Å (300 km s^{-1} blueshift), but no 7323 Å peak is seen. Instead, a smooth red wing is present, not seen in the model, but again reminiscent of the $\text{H}\alpha$ profile.

The 7291 and 7323 Å lines are expected to emit in proportion 3:2 under optically thin circumstances; the upper levels have almost the same excitation energy and collisions between levels 2 and 3 will bring populations close to the 3:2 statistical weight ratio (A -values are the same). However, in the model at 300d, the lines are marginally optically thick ($\tau \sim 1$). Then the luminosity ratio changes from 3:2 towards 1:1.

In the model, the two peaks are separated because the FWHM (800 km s^{-1}) is smaller than the line separation (1310 km s^{-1}). Precisely such a double-peaked feature is seen in SN 1997D at +351 (Fig. 12), and in SN 2008bk (see the next section). Clearly, this is not the situation in SN 2005cs (the line profile stays the same also in the last spectrum at +333d). A smooth structure with a clear weighting of the observed blend towards 7291 Å suggests (a) optical thinness and (b) that the lines are broad enough to blend. Both properties would follow naturally from a larger emitting region, as also suggested by the blue wing of $[\text{Ca II}]$ 7291. The 7291 and 7323 Å lines are separated by 1310 km s^{-1} , and blending will occur at about half this value for the expansion velocity, meaning one needs $V_{\max} \gtrsim 600 \text{ km s}^{-1}$ to avoid it. Finally, some selective suppression of the red wing of 7323 Å, and possibly also 7291 Å, is needed.

Narrow $[\text{Ca II}]$ is produced by mainly the inner ^{56}Ni and O shells, where the newly made Ca resides. Thus, the discrepancy for $[\text{Ca II}]$ means a discrepancy for this innermost region in the model.

Ca II triplet. The triplet is strong both observationally and in the model (Fig. 16 shows a zoom-in). In the observed spectrum the 8498 Å line has scattered in the 8542 Å line, whereas in the model this scattering has not occurred. The red wing of 8542 line indicates again asymmetry with a maximal emission velocity of 2500 km s^{-1} . The line shows a clear flat-topped over about $\pm 500 \text{ km s}^{-1}$. The model line is too narrow, with FWHM of $\sim 900 \text{ km s}^{-1}$.

Nickel. There is no stable nickel in the model (except a solar abundance added in the H envelope). $[\text{Ni II}]$ 7378 is not clearly observed, although there is a red smeared tail of the $[\text{Ca II}]$ doublet. Fig. 17 shows a zoom-in on the 7000–7600 Å region, and a Gaussian fitting as described in Jerkstrand et al. (2015a). A firm upper limit $L_{7378}/L_{7155} < 1$ can be put, which corresponds to a Ni/Fe ratio of solar or less. Thus, we see no indication of the high Ni/Fe production

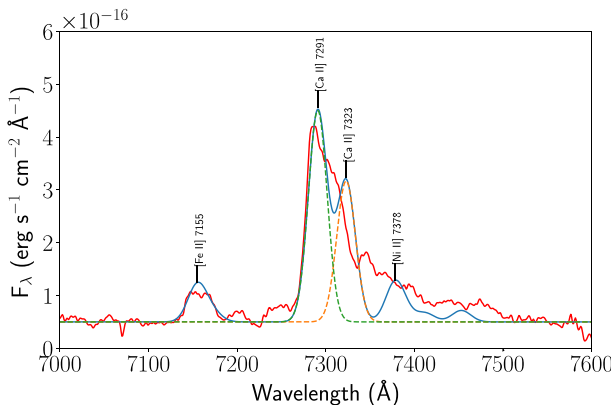


Figure 17. The 7000–7600 Å region in SN 2005cs (red) at +277d, and the Fe, Ca, Ni Gaussian fits described in Jerkstrand et al. (2015b) (blue). From these fits a limit $L_{7378}/L_{7155} \leq 1$ can be put.

that occurs in the inner neutrino-heated ejecta in ECSNe and low-mass CCSNe (Wanajo, Janka & Müller 2011; Wanajo et al. 2017). This conclusion is supported by non-detection of [Ni II] 1.94 μm line (Fig. 15). The nickel abundance is further addressed in more detail in Section 7.

Iron. The observed [Fe II] 7155, 7172 line has a box-like shape (Fig. 16), with expansion velocity of about 600 km s⁻¹. With the telescope resolution limit of 300 km s⁻¹ kept in mind, this emission may arise from a shell at $V \sim 500$ km s⁻¹.

While detection of Fe I 8047, 8075 and Fe I 8204 lines give impetus to confirming presence of Fe in the ejecta, equally strong predicted lines of Fe I 7912, 8307/8310 and 8372/8382 Å are not clearly observed. The problem of identifying Fe is made worse by several overproduced lines at bluer wavelengths, and that the observed line at 8204 Å has a quite strong absorption trough, suggesting a P-Cygni formation. Looking into the model, Na I 8194 is optically thick out to about 1100 km s⁻¹ at 300d. As the model underestimates the scattering in Na I D and Ca II 8542, it is possible that it underestimates the scattering in Na I 8194. Overall it remains ambiguous whether the ⁵⁶Ni component of the model is in fact detected or not.

Fig. 16 shows that Fe I 8204 and Fe I 8347, 8375 do not show the same flat-topped inner regions as lines from H and Ca. This gives some further weight to the hypothesis that this is indeed deep-lying synthesized iron.

6.2.3 Discussion

Signature of He core. From Section 4.1, we know that the He core material imprints signatures of He I 7065, [C I] 8727, [C I] 9850, O I 7774, Fe I 5950 and Fe I lines at 7900–8500 Å, with the Fe I and C I lines the most distinct. The same comparison at 300d (not shown) shows a similar pattern, although now O I 7774 is also made by the H-zone model.

In SN 2005cs at +277d there is no observation of He I 7065, O I 7774 or Fe I 5960. There is, however, observation of most of the Fe I lines in the 7900–8500 Å range (see above), and [C I] 8727. [C I] 9850 is not clearly seen but this lies at the end of the spectrum. Some other weaker Fe I lines in the 8800–9500 Å range are also reasonably well reproduced. Thus, there appears to be signatures of some of the He core material (Fe and C), but not all (O and He). The presence of a He/C zone is ambiguous; [C I] 8727 appears to be seen, but He I 7065 is not seen at all.

The last spectrum at +333 (not shown here) shows no particular differences to the +277d spectrum; no new lines have emerged and the line profiles stay roughly the same.

The most important conclusions we draw from the analysis above are as follows:

(i) The spectral fit of the $9 M_\odot$ model is not particularly good, and further explosion models need to be considered for SN 2005cs. The spectral lines of H and Ca show evidence for significant asymmetry (enhanced receding side emission), something not seen in either SN 1997D or SN 2008bk (next section), and the emission seems to come from a more extended velocity range.

(ii) Attempts to determine whether certain composition zones are present or not are inconclusive. There is no clear evidence for a O shell in the SN, still at +333d after explosion. A He shell is indicated as detected by [C I] lines, but contraindicated by absence of He lines.

(iii) The Ni/Fe production ratio seems low, which is inconsistent with the theoretical nucleosynthesis in ECSNe and lowest mass Fe CCSNe.

The model fits are not quite good enough to claim a strong association of SN 2005cs with a low-mass Fe CCSN. The blue regions have too much line structure and are too bright (although the large uncertainty in data should be kept in mind), and the metal lines from the O and He shells are not in very good agreement. SN 2005cs maintains a rather smooth spectrum even 300d post-explosion, with few hints to its ejecta composition.

6.3 SN 2008bk

SN 2008bk was discovered by Monard (2008) on 2008 March 25 (MJD 54550), in NGC 7793. Photometric data for the first 400d, and spectroscopy up to day 190, were presented in Van Dyk et al. (2012), and photometry at later epochs in Van Dyk (2013). Here, we study a nebular spectrum taken on 2009-09-05 (MJD 55079 = +531d post-explosion, assuming MJD 54548 for explosion epoch) presented in Maguire et al. (2012) (available on WiseRep).

Extinction. No Na I D absorption lines were seen, which suggests low host extinction (Van Dyk et al. 2012). This is also supported by low average extinction of the host galaxy, and dim MIR emission at the site of SN 2008bk. Van Dyk (2013) infers also a low average extinction $A_V = 0.05$ towards the echo of the SN. Higher extinctions were preferred in modelling of the progenitor photometry. Mattila et al. (2008) infer $E(B - V) = 0.3$ mag towards the progenitor, but it is unclear how much of this is due to circumstellar dust that would be destroyed in the explosion. The Milky Way extinction is small, $E(B - V) = 0.02$ mag. Given the tension in results for the host extinction, we deredden here with only this foreground extinction $E(B - V) = 0.02$ mag.

Distance and recession velocity. We use the median distance reported at NED of 3.7 Mpc. The standard deviation is 0.7 Mpc. For recession velocity we adopt 226 km s⁻¹ (NED).

Calibration to photometry. The raw spectrum has synthetic $V = 20.03$ and $I = 19.69$. This compares to $V = 20.10$ and $I = 19.32$ photometry in Van Dyk (2013) at a very similar epoch. I band is difficult for emission line spectra with strong Ca lines, and V band is more relevant for calibration. As the agreement in V band is within the error bar of the photometry, we do not perform any scaling but retain knowledge that there should not be any significant slit losses or other calibration effects.

⁵⁶Ni mass estimate. There is no refereed publication with a ⁵⁶Ni mass estimate of SN 2008bk. In a conference poster,

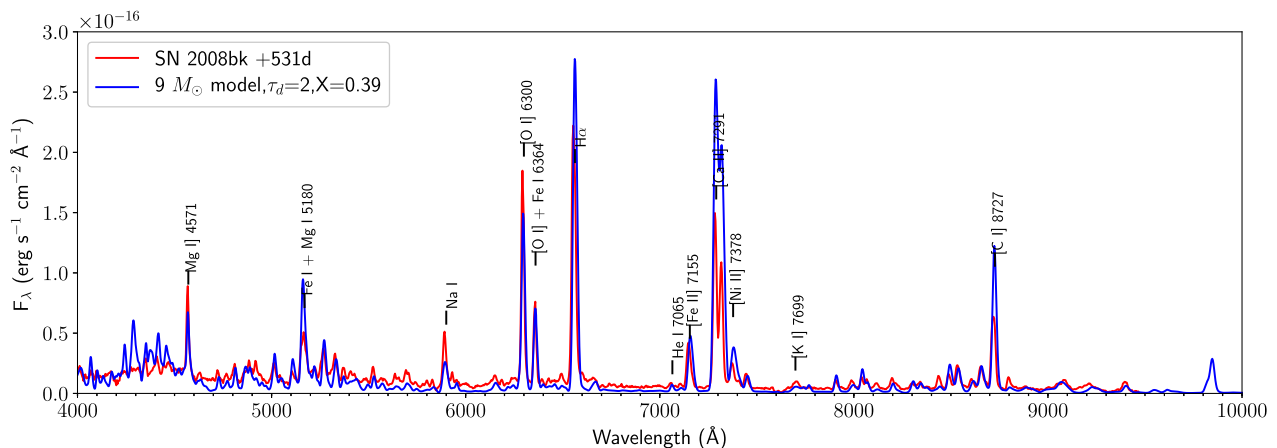


Figure 18. SN 2008bk at +513d (red) compared to the $9 M_{\odot}$ model (blue). The model spectra have been convolved with a Gaussian with FWHM = 10 Å ($\sim 600 \text{ km s}^{-1}$) to match the telescope resolution.

Pignata (2013) (who also assumed $E(B - V) = 0.02$ mag) estimated $M(^{56}\text{Ni}) = 0.009 M_{\odot}$.

Convolution to telescope resolution. The VLT spectrum is stated to have a resolution of 10 Å in Maguire et al. (2012), corresponding to 600 km s^{-1} at 5000 Å. The model spectra were therefore convolved with a Gaussian with FWHM of 10 Å throughout. Note that this gives somewhat broader model lines than in the SN 2005cs comparison, where data had a higher resolution.

6.3.1 Dust formation

The optical light curve of SN 2008bk started declining significantly faster than ^{56}Co after ~ 400 d (fig. 2 in Van Dyk 2013), suggesting the possibility of dust formation. After ~ 600 d the light curves flattened again, suggesting that the bulk of dust formation was over. The dust formation then occurred on similar time-scales as in SN 1987A (Lucy et al. 1989). Pignata (2013) similarly infers beginning of dust production at 490d from the spectroscopic evolution. We note that the similarity between SN 2008bk and SN 1997D and SN 2005cs probably means that dust is not a factor in the interpretation of the < 350 d spectra for these previous sections.

At 531d the blueshifts are of order 300 km s^{-1} . The blueshift is consistently seen in Mg I 4571, H α , [O I] 6300, 6364, [Fe II] 7155 and [Ca II] 7291, 7323, and in several more. The similar effect seen in all lines suggest: (a) Emitting and absorbing material is distributed in a similar manner for Mg, O, H, Fe, Ca, suggesting large-scale mixing. (b) The dust behaves as a grey absorber, which is most easily explained by a distribution of optically thick clumps (Lucy et al. 1989).

A peak blueshift of 300 km s^{-1} on lines expanding with 1000 km s^{-1} corresponds to $\tau_d = 1$ in a uniform sphere model. For a 700 km s^{-1} sphere (ratio becomes 0.45), it corresponds to $\tau_d = 2$. Thus, the indication is extinction with something of this order ($\tau_d = 1 - 2$). We here compare the data to a model with $\tau_d = 2$. Dust likely explains why the optical 531d spectrum is significantly weaker than expected for a ^{56}Ni mass of $0.009 M_{\odot}$; some 3/4 of the luminosity is probably emitted by dust in the IR.

6.3.2 +531d

In Fig. 18, the observed spectrum is compared to model 9 at 500d, with $\tau_d = 2$, and with a further factor $X = 0.39$ to

reach overall optical flux agreement. We make the following observations:

(i) *The [C I] 8727 line is distinctly observed, and within a factor 2 of the model prediction.* The [C I] 8727 line is clearly seen in the observations, which confirms the presence of carbon in the ejecta. The factor 2 overproduction is similar to SN 2005cs (Fig. 14). There is also a (weak) He 7065 present, which further strengthens the presence of a He/C shell.

(ii) *The [Ca II] 7291, 7323 lines are seen with clear separation, indicating low-velocity emitting material as in the model.* The model luminosities are too high by a factor of 2. These lines have contributions from many parts of the ejecta, but there is in particular a strong broad contribution from primordial Ca in the H envelope (Fig. 9, this contribution also grows from 400d to 500d) that is overproduced. It therefore appears unlikely that the energy deposition in the H-rich gas is too low in the model (e.g. we cannot solve the overproduction of [C I] 8727 by transferring gamma energy to the H zone). We cannot reduce it too much either because then H α would become too weak.

(iii) *Synthesized Fe (from ^{56}Ni) is clearly detected in the observed spectrum, from the Fe I 7912, Fe I 8047, 8075, Fe I 8204 and Fe I 8307, 8310 lines.* These lines are in excellent agreement with the model prediction, and completely lacking in the corresponding pure H-nebula model at this epoch, confirming them as unique signatures of the ^{56}Ni region. These Fe I lines show maximum expansion velocities of $\sim 800 \text{ km s}^{-1}$, and FWHM $\sim 1000 \text{ km s}^{-1}$, which, given the telescope broadening, means that the bulk of the ^{56}Ni resides inside $\sim 500 \text{ km s}^{-1}$. This provides important direct constraints on the distribution of ^{56}Ni .

(iv) *[O I] 6300, 6364 is well reproduced.* At this epoch these lines are almost entirely due to O, with little Fe contamination. About 1/3 comes from the H zone, and 2/3 from synthesized oxygen. This success means that this low-mass model, with just $0.07 M_{\odot}$ of oxygen in the ejecta (mostly primordial), passes one critical test for matching low-velocity Type II SNe. As this unmixed 1D setup gives efficient gamma deposition in the thin O shell compared to mixed models, an underproduction would have posed serious problems to account for the [O I] lines (mixing can reduce the line strengths but not easily increase them). We cannot yet say if this success survives in 3D, or what level of agreement more massive ejecta models would give, but for now can state that the model passes the test at this point.

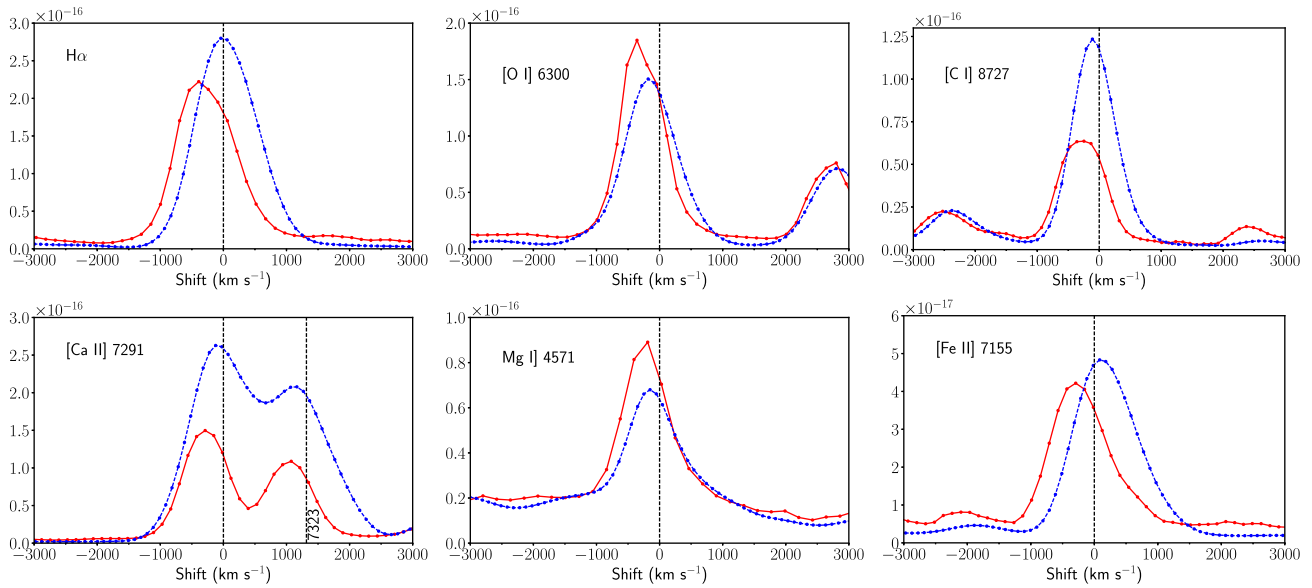


Figure 19. Line profiles in SN 2008bk at +531d. Red solid is the data and blue dashed is the model.

Some further arguments can however be derived from analytic considerations of the oxygen doublet. From the observed 3:1 ratio, the [O I] lines are optically thin at 500d. We may use this result to put an upper limit of the number density using the Sobolev optical depth formula

$$n_{\text{OI}} < \tau 8\pi \frac{g_1}{g_u} A^{-1} \lambda^{-3} t^{-1}, \quad (3)$$

where n_{OI} is the number density of O I, g_1 and g_u are the statistical weights to lower and upper levels, A is the Einstein A value, λ is the wavelength and t is time. For $\tau < 0.1$ and $t = 500$, we get $n_{\text{OI}} < 4 \times 10^7 \text{ cm}^{-3}$. The mass is, letting f denote the filling factor,

$$M_{\text{OI}} = n_{\text{OI}} \frac{4\pi}{3} V^3 t^3 f < 0.18 f M_\odot, \quad (4)$$

where we have used $V < 1000 \text{ km s}^{-1}$. As $f < 1$ the maximum O I mass responsible for the observed [O I] lines is $< 0.18 M_\odot$. Allowing for molecules to have extinguished the optical thermal emission from O/C and O/Si compositions, $0.18 M_\odot$ corresponds to the O/Mg zone in a progenitor of maximum $M_{\text{ZAMS}} = 12 M_\odot$ (Woosley & Heger 2007). This makes it unlikely that high-mass models would be able to reproduce the O lines in SN 2008bk; such stars would give 1:1 ratios for the doublet lines for these low expansion velocities. The same conclusion can be drawn for SN 1997D, which had 3:1 ratio at +480d.

(v) *Mg I] 4571 is well reproduced.* As for the [O I] lines, the suitability of the properties of the O/Mg shell in the model is confirmed. While much of the [O I] line luminosity may be recovered in the H-nebula model, this is not true for the Mg I] 4571 line, providing evidence that there is synthesized material present. Note that the Mg I/Fe I/Fe II 5180 blend is mainly due to Fe II 5160 in the envelope at this epoch. In this spectrum of SN 2008bk, this line is in fact the strongest in the window between Mg I] 4571 and Na I D, providing confirmation that there should be a strong line at this wavelength, although comparisons to SN 1997D and SN 2005cs suggest it emerges too early in the model.

(vi) *[Ni II] 7378 is distinctly seen in the observed spectrum.* It is quite weak, and the model, which has only primordial nickel in the H envelope, overproduces the line, suggesting small amounts

of newly made nickel. This issue is addressed in more detail in Section 7. In the model, almost all of [Fe II] 7155 is from primordial iron at this epoch, and a similar situation would be expected to hold for [Ni II] 7378.

6.3.3 Discussion

Signature of He core. There are clear signatures of the He core from Mg I] 4571, [O I] 6300, 6364, [C I] 8727 and the Fe I lines at 7900–8500 Å. The O, Mg and C lines rule out an ECSN model, and SN 2008bk is again best explained as a Fe CCSN.

Fig. 19 shows zoom-in on selected line profiles. Our simplified treatment of dust does not give the right deformation of line profiles. Some blueshift is obtained for He core lines ([O I] 6300, 6364, [C I] 8727, Mg I] 4571), although too little ($\sim 200 \text{ km s}^{-1}$) compared to the observed shifts (300 – 400 km s^{-1}). For lines mainly coming from the H envelope ($\text{H}\alpha$, [Fe II] 7155) there are no shifts at all in the model, as the dust lies interior to the emitting shell and this does not give blueshifts. The observed shifts in these lines are as strong as for the other lines, and this indicates that the dust distribution should overlap also with H-zone material. We hope to return to more detailed modelling of these line profiles in a future publication where 3D effects and more detailed dust treatment will have to be considered.

7 SENSITIVITY TO EXPLOSIVE NUCLEOSYNTHESIS

The detailed composition of the inner explosively burnt region is not very accurate in the 13-element alpha network in P-HOTB. Here, we consider sensitivity to this composition by analysis of models with hand-made composition changes guided by more detailed simulations of the burning in this region.

Wanajo et al. (2009) presented detailed post-processing nucleosynthesis calculations of the 1D ECSN simulation of Kitaura, Janka & Hillebrandt (2006). The ejecta obtain an electron fraction in the range $Y_e = 0.47$ – 0.53 (see Wanajo, Janka & Müller 2011 for figure), with an average value below 0.5 and significant

production of neutron-rich isotopes such as ^{58}Ni and ^{60}Zn . In each mass shell of the Wanajo et al. (2009) model, the dominant isotope is ^{56}Ni , ^{58}Ni or ^{60}Ni .

The total yields in this model of the most common elements are He ($5.12 \times 10^{-3} M_{\odot}$), $^{58,60,62}\text{Ni}$ ($4.39 \times 10^{-3} M_{\odot}$), $^{56}\text{Ni}/^{56}\text{Fe}$ ($2.50 \times 10^{-3} M_{\odot}$) and $^{64,66}\text{Zn}$ ($1.09 \times 10^{-3} M_{\odot}$), together making up $1.31 \times 10^{-2} M_{\odot}$ or 94 per cent of the mass of the explosively burnt and neutrino-processed region, in (normalized) mass fractions 0.46 (He), 0.40 (Ni), 0.22 (Fe) and 0.09 (Zn). In our standard 13-element $9 M_{\odot}$ model, these mass fractions are instead 0.72 (He), 0 (Ni), 0.25 (Fe) and 0 (Zn). Only a negligible fraction ($< 10^{-15}$) of the ^{56}Ni remains undecayed at nebular times, but a few percent of the ^{56}Co remains undecayed (7 per cent at 300d and 1 per cent at 500d), also giving a cobalt mass fraction of about 1 per cent. The Ni/Fe and Zn/Fe ratios in the Wanajo et al. (2009) model are 32 and 310 times their solar values, and these elements may therefore be unique signatures of ECSN nucleosynthesis.

Wanajo, Janka & Müller (2011) followed up by computing the nucleosynthesis for the same progenitor exploded in 2D. The 2D model showed roughly the same Y_e distribution, except that a low- Y_e tail was created. There were only minor (< factor 2) differences in yields for elements with $Z < 34$ (see their fig. 3). For some heavier elements ($Z = 34\text{--}40$) larger variations were seen, but these elements still remain too rare to have any visible emission in the nebular spectra. Thus, we conclude the 1D yields for He, Fe, Ni and Zn from Wanajo et al. (2009) can be used to good accuracy.

Wanajo et al. (2017) expanded these 2D simulations to iron cores. It was found that the lowest mass iron cores ($M_{\text{ZAMS}} = 8.1, 9.6 M_{\odot}$) produce nucleosynthesis very similar to the ECSNe of Wanajo et al. (2009) and Wanajo, Janka & Müller (2011), implying that ECSNe cannot be uniquely identified based on signatures from their explosive nucleosynthesis. For more massive iron cores ($M_{\text{ZAMS}} = 11, 15, 27 M_{\odot}$), on the other hand, slower shock expansion led to significantly higher Y_e values and lower production of neutron-rich isotopes. Therefore, high Ni/Fe and Zn/Fe ratios appear to be at least diagnostic of the lowest mass range ($\sim 8\text{--}10 M_{\odot}$), giving EC-SNe or ECSN-like explosions.

None of these specific models are available to us to use here as they were not evolved into the homologous phase. Instead, to mimic such a structure, we created a variant of the $9 M_{\odot}$ model (without beta decay effects) in which the inner region, taken as where the ^{56}Ni fraction exceeded 10 per cent, had some of the helium in the explosive region removed and replaced by ^{58}Ni giving $^{58}\text{Ni}/^{56}\text{Ni} = 3$ and 20 times solar (this was done in each zone where the ^{56}Ni mass fraction was over 1 per cent). Note that beyond this added nickel, there is also primordial nickel in the hydrogen zone. SUMO does not currently treat zinc, and we therefore have to defer study of zinc abundance. The He abundance was correspondingly reduced to ensure mass fractions added to unity. These model were computed at 300d (for comparison with SN 2005cs) and at 500d, with dust optical depth $\tau_d = 2$ (Section 2.2) for comparison with SN 2008bk.

7.1 SN 1997D

Fig. 20 (top) shows a comparison between the model at 300d and SN 1997D at 350d, zoomed in at the two regions containing the only major changes to the optical spectrum: [Ni II] 6667 and [Ni II] 7378, 7412. While [Ni II] 7378 initially shows promise for a high Ni/Fe ratio, the observed [Ni II] 7412 and [Ni II] 6667 lines are clearly too dim for such a high ratio. In the model at 400d, the [Ni II] 7378 line has emerged more prominently in the Ni/Fe = 0 model (from

primordial nickel in the envelope), and the overall analysis therefore strongly points to Ni/Fe between 0 and 3 times solar.

The figure illustrates that while the Ni lines grow in strength with increased abundance in the explosive region, the growth is quite slow. This is because the lines become optically thick. As an illustration of the line formation, in the model with 20 times Ni/Fe, the Ni II fraction is 0.7 at 200 km s^{-1} (very similar to Fe value), and Ni II contributes 6 per cent to the cooling (compare 70 per cent in Fe I and 5 per cent in Fe II). The optical depths are 7.1 in [Ni II] 7378, 2.4 in [Ni II] 7412 and 1.7 in [Ni II] 6667. This optical depth means that the difference between the model with Ni/Fe = 3 and Ni/Fe = 20 is much smaller than 20/3.

The very strong [Ni II] 7378 in the Crab nebula has been taken as an argument for a very high Ni/Fe ratio and an origin in the $8\text{--}10 M_{\odot}$ range. At the much higher age of the Crab this line has become optically thin and is therefore a more direct diagnostic of the stable nickel content. Nevertheless, the diagnostic is still powerful enough here to rule out a high Ni/Fe ratio in SN 1997D.

7.2 SN 2005cs

Fig. 20 (middle) shows a comparison between the models and SN 2005cs at 300d. While there is a broad emission region between 7350 and 7600 \AA seen in the data, the distinct bump expected for [Ni II] 7378, 7412 is not present. The discrepancy for [Ni II] 6667 is even clearer, and again a Ni/Fe ratio as high as 20 is disfavoured.

7.3 SN 2008bk

Fig. 20 (bottom) shows a comparison with SN 2008bk at 531d. The analysis here is complicated by the dust formation, which eats away at line profiles and is not modelled in detail with our simplistic dust treatment.

At these later epochs, there is less deposition in the inner region (20 per cent), the gas is more neutral ($x_e = 0.04$) and colder ($T = 3000 \text{ K}$), and so the nickel lines from synthesized nickel are weaker compared to 300d. There is therefore a smaller difference for the three models. [Ni II] 6667 is predicted too weak to observe even at Ni/Fe = 20.

The emission from primordial nickel in the envelope dominates emission from synthesized nickel, so the models with synthesized nickel are only somewhat brighter in the nickel lines than the model with no synthesized nickel. Note that the temperature and ionization decrease slower, and sometimes even increase, in the envelope compared to the ^{56}Ni core (Figs 5 and 6), so the ratio of emission from primordial to synthesized iron-group elements increase with time. The observed [Ni II] 7378 line is weaker than even the Ni/Fe = 0 model, and thus there is no sign of strong nickel production either in SN 2008bk, although the caveat with dust formation should be kept in mind. The [Ni II] $1.94 \mu\text{m}$ line shows a similar behaviour as the [Ni II] 7378 line.

7.4 Discussion

A caveat to these results is that the fraction of energy absorbed by the ^{56}Ni clumps may vary in a 2D/3D model. Thus, we cannot completely rule out that a high Ni/Fe ratio could be present and still give weak [Ni II] lines, if mixing significantly reduces the local gamma trapping. However, we note that the Fe I lines at $7900\text{--}8500 \text{ \AA}$, whose strength depends on this self-absorption, are relatively well reproduced with the current set-up. Also, in the model at 500d, the fraction of energy absorbed in these clumps is just 8 per cent,

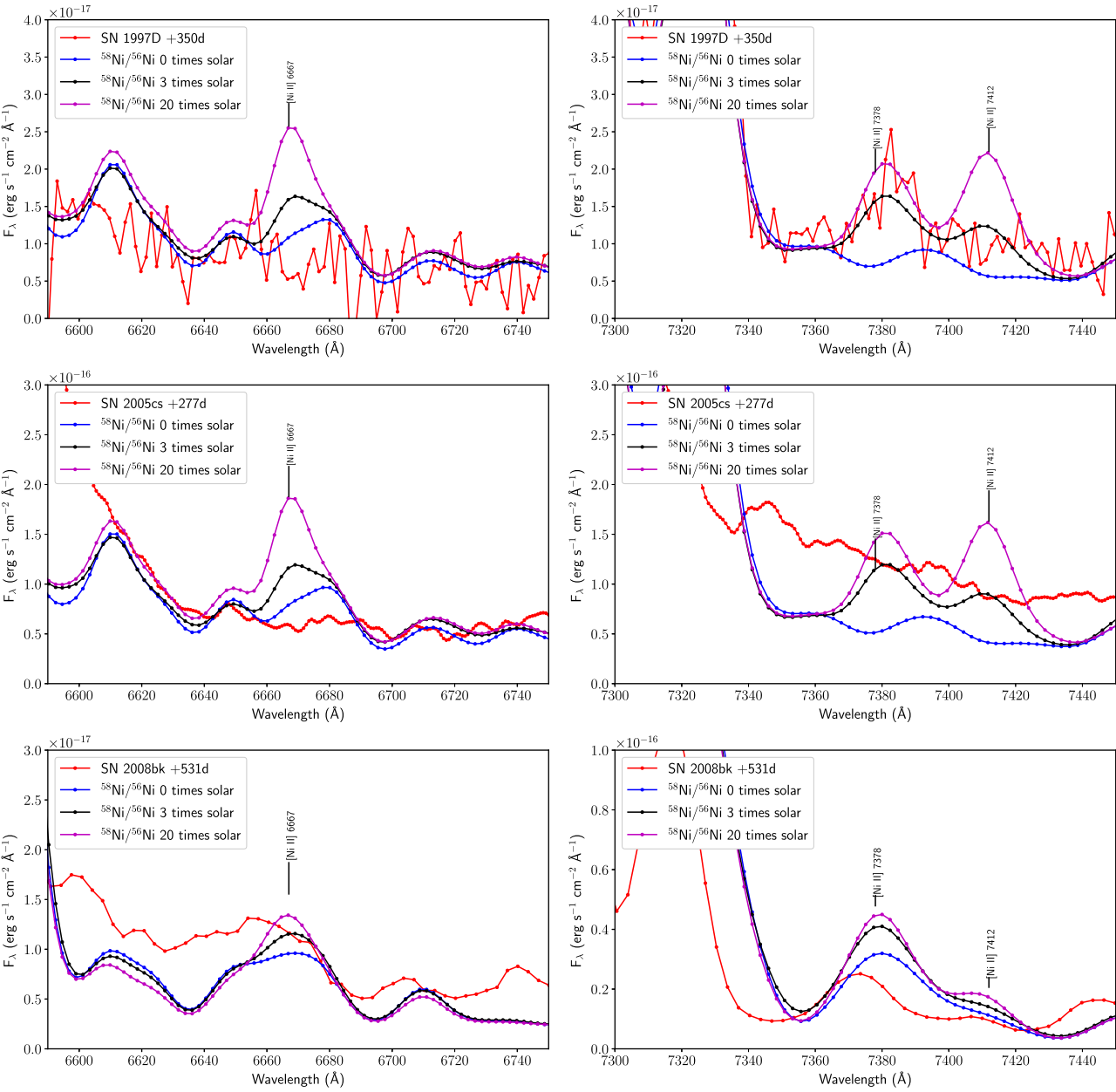


Figure 20. Comparison of models with varying amounts of synthesized stable nickel added in the explosive burning region (as by the stated $^{58}\text{Ni}/^{56}\text{Ni}$ value), and SN 1997D (top), SN 2005cs (middle) and SN 2008bk (bottom). No high production of stable nickel is suggested in either. Ni/Fe = 0 refers to the original model where nickel only exists as a primordial abundance in the H envelope.

and half of this is positron energy which definitely cannot escape. Thus, there should be maximum a factor 2 overproduction of the synthesized component. We therefore think our result here, that none of these three SNe show $\text{Ni/Fe} \gg 1$, and thereby do not originate from ECSN or ECSN-like explosions, is robust.

Neither our P-HOTB nor KEPLER models can make an accurate prediction for Y_e and ^{58}Ni nucleosynthesis, as this requires both a large network and neutrino processed ejecta. Without neutrinos, the KEPLER model gives a Ni/Fe ratio close to solar. Inspection of the Y_e profile in P-HOTB gives some indication of what production of ^{58}Ni can be expected. Fig. 21 shows that Y_e varies significantly within the explosive nucleosynthesis region. Using the charts in Jerkstrand et al. (2015c), we can estimate for the relevant entropies ($S_\gamma/R = 20\text{--}30$) what the ^{58}Ni mass fraction roughly would be (for

KEPLER, the Y_e is close to the one of the progenitor shown in Fig. A1 as it does not include neutrino processes).

Adding the regions together (with the average ^{58}Ni fraction in each zone), the total expected ^{58}Ni production is about $3 \times 10^{-3} M_\odot$, about half the ^{56}Ni production and a Ni/Fe ratio of 8 times solar. This is between the solar production occurring in massive progenitors and the 20–30 times solar value occurring in ECSNe-like explosions.

The simplified neutrino calculation and 1D geometry prevent us from firmly saying whether this would hold true in a more advanced model. A Ni/Fe ratio of 8 would from our comparisons above not fit these three observed candidates, and a more massive model (with lower Ni/Fe) would be preferable ($M_{\text{ZAMS}} \gtrsim 10\text{--}11 M_\odot$). However, it is also possible that this $9.0 M_\odot$ model obtains a lower ^{58}Ni

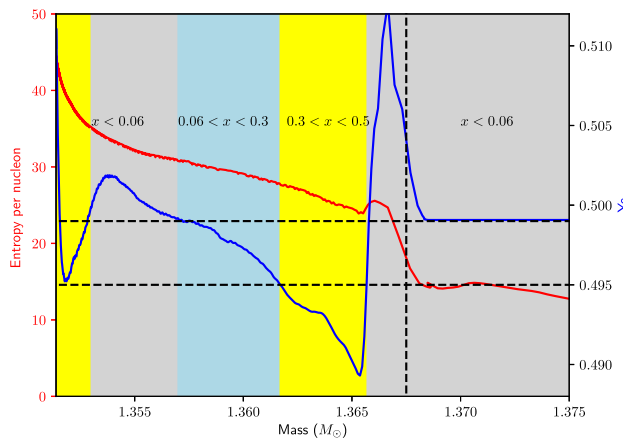


Figure 21. Profiles of Y_e (blue line, right axis) and entropy per baryon (red line, left axis) for the innermost ejecta, at the radial location where $T_9 = 7$ and NSE freezes out. Regions of intervals mapped to the ^{58}Ni mass fraction (shown as x), using the results of Jerkstrand et al. (2015c) are indicated. The vertical dashed line at $M = 1.3675 \text{ M}_\odot$ marks the outer edge of the neutrino processed region. The horizontal dashed lines mark $Y_e = 0.499$ and $Y_e = 0.495$ that were used for mapping. Iron-group production occurs throughout the plotted domain. The left edge of the region is the final mass cut at 1.35138 M_\odot .

production in a multi-D simulation with full neutrino physics (work in progress).

8 DISCUSSION

8.1 Multi-D effects

As our model is 1D, and it has been previously shown that multi-D hydrodynamic effects often are strong in Type IIP SNe, an assessment of the possible impact of mixing effects is warranted. Regarding the explosion itself, a 2D ECSN explosion was simulated by Janka et al. (2008), who demonstrated a weak sensitivity of shock propagation and explosion energy to dimensionality (see also Müller, Janka & Heger 2012; Müller, Janka & Marek 2013, for other published examples). The only 3D simulation done for the low-mass range is by Melson, Janka & Marek (2015), who discuss the impact on explosion energy in a 400 ms simulation of a 9.6 M_\odot progenitor. In 3D a somewhat more rapid explosion occurs compared to 2D, with a 10 per cent higher explosion energy.

These runs were however too short (< 1 s) to reach conclusions on large-scale mixing occurring as reverse shocks are created at later times. If these produce as strong stirring of the inner ejecta as at higher M_{ZAMS} (e.g. Hammer, Janka & Müller 2010), the resulting spectrum, both line profiles and luminosities, can change significantly as the radioactive gamma deposition changes between the different layers. With models using strong mixing, Maguire et al. (2012) and Lisakov et al. (2017) found reasonable fits to SN 2008bk for a 12 M_\odot star. Thus, the precise best-fitting mass likely depends on the amount of mixing.

However, for two reasons we expect less mixing of ^{56}Ni into the He and H layers than in more massive progenitors. First, the explosion energy of $\sim 10^{50}$ erg is considerably lower than the more canonical 10^{51} erg of $15\text{--}20 \text{ M}_\odot$ stars. Secondly, the relative amount of ^{56}Ni and ejecta is also lower ($\sim 0.006/7.5$ compared to $0.07/(13 - 18)$ for massive progenitors). Both facts favour less entrainment of high-velocity ^{56}Ni into the He and H shells. Since the detailed structure of the progenitor star, however, plays a crucial

role for the mixing (Wongwathanarat, Müller & Janka 2015), 3D long-time explosion simulations are needed for a final answer.

We also note that strong mixing would lead to brightening of lines such as $\text{H}\alpha$. In our unmixed set-up the gamma deposition in the H envelope is about 20 per cent at 200d, and this gives a well-reproduced $\text{H}\alpha$ compared to SN 1997D and SN 2005cs (no data on SN 2008bk). This line, and also other lines such as $[\text{Ca II}] 7291, 7323$ would become too strong in a mixed scenario.

The impact on nucleosynthesis going from 1D to 2D for low-mass SNe was studied by Wanajo, Janka & Müller (2011, ECSNe) and Wanajo et al. (2017, low-mass CCSNe). In both cases, the authors find significant differences for some high-A isotopes (see also Yoshida et al. 2017), but for the dominant species that produce the nebular spectra (e.g. Fe, Ni) the differences were small compared to 1D models (Wanajo et al. 2009).

8.2 The link between subluminous IIP SNe and $8\text{--}12 \text{ M}_\odot$ stars

When subluminous Type II SNe were discovered in 1997, one hypothesis put forth was that these were massive stars exploding with a low energy and fall-back of ^{56}Ni (Turatto et al. 1998). From several arguments presented below we consider it more plausible that this observational class is linked to low-mass progenitors.

(i) The observationally inferred explosion energies and amounts of ^{56}Ni are naturally obtained in current ab initio explosion simulations of low-mass progenitors (Kitaura, Janka & Hillebrandt 2006; Melson, Janka & Marek 2015; Müller 2016; Wanajo et al. 2017). If subluminous IIP SNe do not correspond to these progenitors, what observational class would?

(ii) While a single object or two could perhaps be explained by fall-back, extreme fine-tuning would be needed to consistently produce a ^{56}Ni mass of $\sim 5 \times 10^{-3} \text{ M}_\odot$, as observed now in over a dozen objects (Spiro et al. 2014), making up a good fraction of closely studied Type IIP SNe. It has, in addition, not been demonstrated that such fall-back is dynamically possible.

(iii) The observed fraction of these events relative to all Type IIP SNe is of order 1/3 (using fig. 16 in Spiro et al. 2014). This roughly corresponds to the range of $8\text{--}11 \text{ M}_\odot$ if we assume $M_{\text{max}} = 25 \text{ M}_\odot$ for Type IIP SNe (this gives 44 per cent with a standard Salpeter IMF).

(iv) These three cases have direct progenitor detections given low masses, $M_{\text{ZAMS}} = 8\text{--}15 \text{ M}_\odot$.

(v) The nebular model of a low-mass progenitor studied here fits line profiles and luminosities in two out of three events, without any tuning. Even without a model, the evolution of the $[\text{O I}] 6300, 6364$ ratio is not consistent with large amounts of oxygen as originally pointed out by Chugai & Utrobin (2000).

Tension still comes from hydrodynamic light-curve modelling, which occasionally points to higher masses. Two main results are in particular giving substantially higher values; those of Zampieri et al. (2003) and Utrobin & Chugai (2008). The result of Utrobin & Chugai (2008) is for SN 2005cs, which is the object we could not draw any strong conclusions on regarding nucleosynthesis. It has somewhat different line profiles than SN 1997D and SN 2008bk, and may originate from a different kind of progenitor, or have exploded in a different way, perhaps with more mixing.

For very few CCSNe, we have strong constraints on the progenitor star that exploded. Subluminous IIP SNe hold promise to become the observational class where we have a firm idea of the progenitor mass range to within $1\text{--}2 \text{ M}_\odot$. If this is achieved, we can move

on to constrain the stellar evolution and explosion physics by comparing detailed models starting from a narrow range of progenitor masses. Of particular importance here is SN 2008bk, which exploded just 3.7 Mpc away and is firmly indicated to be an $\sim 10 M_{\odot}$ star from both progenitor detection, hydrodynamic modelling and nucleosynthesis analysis. With a large available data set (Pignata, in preparation) this will become an important test-bed for low-mass explosion models.

Another topic we can make progress on now is to attempt to answer whether ECSNe occur in Nature. Recent stellar evolution modelling has indicated that the progenitor mass range is narrow and may not exist at all. Here, we note that zero out of three subluminous IIP SNe shows nucleosynthesis of stable nickel that would be expected from an ECSN (Wanajo *et al.* 2009; Wanajo, Janka & Müller 2011). They also show evidence for He core lines, which would be lacking in ECSNe. While there remains a possibility that some of the He shell emission (He and C lines) may be moved to the H envelope in a progenitor with dredge-up, emission by O shell material should be truly absent in an ECSN.

In a toy scenario where ECSNe would come from the range 8 to $8 + \Delta M M_{\odot}$ stars and subluminous IIP from 8 to $12 M_{\odot}$ stars, we can already make a rough constraint on ΔM by taking $((4 - \Delta M)/4)^3 > p$ (probability p to have zero of three events belong to the ECSN category). This gives $\Delta M < 1.2 M_{\odot}$ on a 1σ level (ignoring IMF weighting). A problem here, though, is that recent 2D models have shown that also the lowest mass Fe CCSNe could produce much stable Ni. Wanajo *et al.* (2017) found similar Ni/Fe ratios of ~ 20 – 30 times solar in e8.8 (ECSN), u8.1(Fe CCSN) and z9.6 (Fe CCSN) models. Note that the (unpublished) u8.1 and z9.6 models have extreme metallicities ($Z = 10^{-4}$ and 0, respectively), and behave differently from other models in this mass range. For example, the density profile of z9.6 model is much steeper than for the $9.0 M_{\odot}$ model we have considered here, despite its higher mass (see e.g. fig. 1 in Radice *et al.* 2017).

At $M_{\text{ZAMS}} = 11.2 M_{\odot}$, the Ni/Fe ratio was restored to close to solar in Wanajo *et al.* (2017). It is of importance to investigate what happens in solar metallicity Fe CCSN models at 9 – $11 M_{\odot}$, which have density gradients between the z9.6 and 11.2 models. If these also produced high Ni/Fe ratios, it would become an issue that we do not observe strong ^{58}Ni lines in any of these objects. We note here that several uncertainties in the neutrino treatment, e.g. neutrino oscillations, also leave some uncertainty for the calculations of these yields.

8.3 The existence of faint supernovae from massive stars

The high masses inferred for some subluminous Type IIP SN by hydrodynamic modelling led to the hypothesis of two branches of SNe in the $M_{\text{ZAMS}}\text{--}E$ plane; the bright and faint branches (Nomoto, Kobayashi & Tominaga 2013). One important observational puzzle that the existence of a faint branch could solve is the abundances of CEMP stars, which are enriched in intermediate elements like C and O, but lack iron-group elements. Only a fall-back SN from a massive star could easily explain these.

As discussed above, we think there is overall scant evidence for the existence of such a branch in the local Universe. In particular, nebular spectra of SN 1997D do strongly suggest a low-mass star, and there is almost no data on the photospheric phase to constrain light-curve models.

One attractive scenario would be that faint supernovae occurred in the early Universe, but not today. Indeed low metallicity makes it harder to explode stars, and fall-back cases might become more likely (Pejcha & Thompson 2015).

9 CONCLUSIONS AND SUMMARY

We have calculated the spectral appearance of a $9 M_{\odot}$ CCSN in the interval 200–600d post-explosion, using a neutrino-driven 1D model. We analysed the spectral formation processes in this model, and compared the model spectra with observed spectra of subluminous Type IIP SNe. Our main conclusions are as follows:

- (i) After radioactive decays, the He core in a low-mass Type IIP SN producing $\sim 5 \times 10^{-3} M_{\odot}$ of ^{56}Ni expands with $\sim 500 \text{ km s}^{-1}$. Inclusion of the ‘Ni bubble’ effect broadens lines by a factor ~ 2 and changes some line luminosities.
- (ii) Gamma-rays are fully trapped for about 3 yrs, giving a light curve following the ^{56}Co decay for this amount of time. The gamma-rays are absorbed in the innermost 500 – 1000 km s^{-1} of the ejecta, which leads to emission lines with FWHM $\sim 900 \text{ km s}^{-1}$ for He core lines (when convolved with typical telescope resolution of 300 km s^{-1} , this becomes 950 km s^{-1}), and somewhat larger for H lines ($\sim 1100 \text{ km s}^{-1}$).
- (iii) Despite the low mass of ^{56}Ni , O and He zones compared to the H zone, these shells absorb significant amounts of gamma-ray energy and emit characteristic, detectable signatures:
 - (a) The ^{56}Ni shell displays unique Fe I lines in the 7900 – 8500 \AA range.
 - (b) The He shell displays unique He I 7065 and $[\text{C I}]$ 8727.
 - (c) The O shell displays unique O I 7774, and enhances Mg II 4571 and $[\text{O I}]$ 6300, 6364.
- (iv) The $9 M_{\odot}$ explosion model, without any free parameters except a rescaling factor of order 2 to allow for somewhat different ^{56}Ni masses, gives good reproduction of nebular spectra of subluminous Type IIP SN 1997D and SN 2008bk, associating this class with the lowest mass end of the progenitor spectrum. Both line profiles and luminosities naturally emerge at their observed values when an explosion delivers $\sim 0.1 \text{ B}$ to a low-mass progenitor. While high-mass models have not yet been calculated, one can find arguments against them from certain line ratios. In addition, even if such suitable models can be constructed, they would require fine-tuning to get the right amount of fall-back and core structure.
- (v) For SN 2005cs, the link cannot be as clearly established as by the end of the observational coverage at $+330\text{d}$, key diagnostic lines of e.g. Mg I 4571, $[\text{O I}]$ 6300, 6364 had still not emerged (this happened sometime between $+207$ and $+350\text{d}$ in SN 1997D and between $+265\text{d}$ and $+416\text{d}$ in SN 2008bk). However, spectral similarities to SN 2008bk around 265d are high, which make a common scenario plausible.
- (vi) None of the observed events show the high Ni/Fe ratio (~ 30 times solar) predicted for ECSN and ECSN-like explosions. SN 1997D and SN 2008bk also show clear evidence of He core material, which consistently rules out ECSN models for them. Thus, we assess that ECSNe remain to be discovered from spectroscopic analysis, and we note here that the expected signature is *lack* of certain lines (He I 7065, $[\text{C I}]$ 8727, Mg I 4571) at $t \gtrsim 350\text{d}$, combined with strong $[\text{Ni II}]$ 6667 and $[\text{Ni II}]$ 7378. With zero of three subluminous IIP objects matched to ECSN nucleosynthesis, their progenitor mass range is constrained to $\Delta M \lesssim 1 M_{\odot}$ at 1σ .
- (vii) With very good consistency with spectral modelling performed here, progenitor detection, and light-curve modelling, SN 2008bk is today perhaps most robustly inferred explosion of a low-mass Fe CCSN, with $M_{\text{ZAMS}} = 9$ – $12 M_{\odot}$. This gives strong empirical support for the developing theoretical picture that low-mass stars explode with a low energy ($\sim 0.1 \text{ B}$) and a low ^{56}Ni mass ($\sim 5 \times 10^{-3} M_{\odot}$). The close distance (3.7 Mpc) and a comprehensive data set will allow this SN to become a test-bed for detailed

stellar evolution/explosion models for the 9–12 M_⊙ range, similar to what SN 1987A has been for ∼20 M_⊙ progenitors.

ACKNOWLEDGEMENTS

We thank the anonymous referee for careful reading and useful comments and suggestions. We thank A. Pastorello, L. Siess, K. Nomoto, B. Müller and L. Tomasella for useful discussions. AJ acknowledges funding by the European Union’s Framework Programme for Research and Innovation Horizon 2020 under Marie Skłodowska-Curie grant agreement No. 702538.

REFERENCES

- Barklem P. S., Osorio Y., Fursa D. V., Bray I., Zatsariny O., Bartschat K., Jerkstrand A., 2017, *A&A*, 606, A11
- Baron E., Branch D., Hauschildt P. H., 2007, *ApJ*, 662, 1148
- Benetti S. et al., 2001, *MNRAS*, 322, 361
- Botticella M. T. et al., 2009, *MNRAS*, 398, 1041
- Brown P. J. et al., 2007, *ApJ*, 659, 1488
- Chugai N. N., Utrobin V. P., 2000, *A&A*, 354, 557
- de Mello D., Benetti S., Massone G., 1997, *IAU Circ.*, 6537
- Dessart L. et al., 2008, *ApJ*, 675, 644
- Dessart L., Hillier D. J., Waldman R., Livne E., 2013, *MNRAS*, 433, 1745
- Doherty C. L., Gil-Pons P., Siess L., Lattanzio J. C., Lau H. H. B., 2015, *MNRAS*, 446, 2599
- Eldridge J. J., Tout C. A., 2004, *MNRAS*, 353, 87
- Eldridge J. J., Mattila S., Smartt S. J., 2007, *MNRAS*, 376, L52
- Falke S., Tiemann E., Lisdat C., Schnatz H., Grosche G., 2006, *Phys. Rev. A*, 74, 032503
- Fransson C., Chevalier R. A., 1989, *ApJ*, 343, 323
- Fraser M. et al., 2011, *MNRAS*, 417, 1417
- García-Berro E., Ritossa C., Iben I., Jr, 1997, *ApJ*, 485, 765
- Hammer N. J., Janka H.-T., Müller E., 2010, *ApJ*, 714, 1371
- Hendry M. A. et al., 2005, *MNRAS*, 359, 906
- Herant M., Benz W., 1992, *ApJ*, 387, 294
- Iben I., Jr, Ritossa C., García-Berro E., 1997, *ApJ*, 489, 772
- Janka H.-T., Mueller E., 1996, *A&A*, 306, 167
- Janka H.-T., Müller B., Kitaura F. S., Buras R., 2008, *A&A*, 485, 199
- Janka H.-T., Hanke F., Hüdepohl L., Marek A., Müller B., Obergaulinger M., 2012, *Prog. Theor. Exp. Phys.*, 2012, 01A309
- Jerkstrand A., Fransson C., Kozma C., 2011, *A&A*, 530, A45
- Jerkstrand A., Fransson C., Maguire K., Smartt S., Ergon M., Spyromilio J., 2012, *A&A*, 546, A28 (J12)
- Jerkstrand A., Smartt S. J., Fraser M., Fransson C., Sollerman J., Taddia F., Kotak R., 2014, *MNRAS*, 439, 3694 (J14)
- Jerkstrand A. et al., 2015a, *MNRAS*, 448, 2482
- Jerkstrand A., Ergon M., Smartt S. J., Fransson C., Sollerman J., Taubenberger S., Bersten M., Spyromilio J., 2015b, *A&A*, 573, A12
- Jerkstrand A. et al., 2015c, *ApJ*, 807, 110
- Jones S. et al., 2013, *ApJ*, 772, 150
- Jones S., Hirschi R., Nomoto K., 2014, *ApJ*, 797, 83
- Jones S., Röpke F. K., Pakmor R., Seitenzahl I. R., Ohlmann S. T., Edelmann P. V. F., 2016, *A&A*, 593, A72
- Kitaura F. S., Janka H.-T., Hillebrandt W., 2006, *A&A*, 450, 345
- Kloeck W., Muendlein R., Li W., Yamaoka H., Itagaki K., 2005, *IAU Circ.*, 8553
- Kozma C., Fransson C., 1992, *ApJ*, 390, 602
- Kozma C., Fransson C., 1998a, *ApJ*, 496, 946
- Kozma C., Fransson C., 1998b, *ApJ*, 497, 431
- Lepp S., Dalgarno A., McCray R., 1990, *ApJ*, 358, 262
- Li W., Van Dyk S. D., Filippenko A. V., Cuillandre J.-C., Jha S., Bloom J. S., Riess A. G., Livio M., 2006, *ApJ*, 641, 1060
- Lisakov S. M., Dessart L., Hillier D. J., Waldman R., Livne E., 2017, *MNRAS*, 466, 34
- Lodders K., 2003, *ApJ*, 591, 1220
- Lucy L. B., Danziger I. J., Gouiffes C., Bouchet P., 1989, in Tenorio-Tagle G., Moles M., Melnick J., eds, *Lecture Notes in Physics*, Vol. 350, IAU Colloq. 120: Structure and Dynamics of the Interstellar Medium. Springer-Verlag, Berlin, p. 164
- Maguire K. et al., 2012, *MNRAS*, 420, 3451
- Mattila S., Smartt S. J., Eldridge J. J., Maund J. R., Crockett R. M., Danziger I. J., 2008, *ApJ*, 688, L91
- Mauas P. J., Avrett E. H., Loeser R., 1988, *ApJ*, 330, 1008
- Maund J. R., Smartt S. J., 2009, *Science*, 324, 486
- Maund J. R., Smartt S. J., Danziger I. J., 2005, *MNRAS*, 364, L33
- Maund J. R., Mattila S., Ramirez-Ruiz E., Eldridge J. J., 2014, *MNRAS*, 438, 1577
- Maund J. R., Fraser M., Reilly E., Ergon M., Mattila S., 2015, *MNRAS*, 447, 3207
- Mayle R., Wilson J. R., 1988, *ApJ*, 334, 909
- Meikle W. P. S. et al., 2007, *ApJ*, 665, 608
- Melson T., Janka H.-T., Marek A., 2015, *ApJ*, 801, L24
- Miyaji S., Nomoto K., Yokoi K., Sugimoto D., 1980, *PASJ*, 32, 303
- Monard L. A. G., 2008, *Central Bureau Electronic Telegrams*, 1315
- Moriya T. J., Eldridge J. J., 2016, *MNRAS*, 461, 2155
- Moriya T. J., Tominaga N., Langer N., Nomoto K., Blinnikov S. I., Sorokina E. I., 2014, *A&A*, 569, A57
- Müller B., 2016, *PASA*, 33, e048
- Müller B., Janka H.-T., Heger A., 2012, *ApJ*, 761, 72
- Müller B., Janka H.-T., Marek A., 2013, *ApJ*, 766, 43
- Nomoto K., 1984, *ApJ*, 277, 791
- Nomoto K., 1987, *ApJ*, 322, 206
- Nomoto K., Kobayashi C., Tominaga N., 2013, *ARA&A*, 51, 457
- Pastorello A. et al., 2004, *MNRAS*, 347, 74
- Pastorello A. et al., 2006, *MNRAS*, 370, 1752
- Pastorello A. et al., 2009, *MNRAS*, 394, 2266
- Pejcha O., Thompson T. A., 2015, *ApJ*, 801, 90
- Pignata G., 2013, *Massive Stars: From Alpha to Omega*. Rhodes, Greece, p. 176
- Piumelli E., Tamborra I., Wanajo S., Janka H.-T., Hüdepohl L., 2015, *ApJ*, 808, 188
- Poelarends A. J. T., 2007, PhD thesis, Utrecht Univ.
- Poelarends A. J. T., Herwig F., Langer N., Heger A., 2008, *ApJ*, 675, 614
- Pumo M. L., Zampieri L., Spiro S., Pastorello A., Benetti S., Cappellaro E., Manicò G., Turatto M., 2017, *MNRAS*, 464, 3013
- Radice D., Burrows A., Vartanyan D., Skinner M. A., Dolence J. C., 2017, *ApJ*, 850, 43
- Ritossa C., Garcia-Berro E., Iben I., Jr, 1996, *ApJ*, 460, 489
- Ritossa C., Garcia-Berro E., Iben I., Jr, 1999, *ApJ*, 515, 381
- Roy R. et al., 2011, *ApJ*, 736, 76
- Siess L., 2006, *A&A*, 448, 717
- Siess L., 2007, *A&A*, 476, 893
- Spiro S. et al., 2014, *MNRAS*, 439, 2873
- Sukhbold T., Ertl T., Woosley S. E., Brown J. M., Janka H.-T., 2016, *ApJ*, 821, 38
- Takahashi K., Yoshida T., Umeda H., 2013, *ApJ*, 771, 28
- Takáts K., Vinkó J., 2006, *MNRAS*, 372, 1735
- Tauris T. M., Langer N., Podsiadlowski P., 2015, *MNRAS*, 451, 2123
- Tomasella L. et al., 2017, *MNRAS*, preprint ([arXiv:1712.03933](https://arxiv.org/abs/1712.03933))
- Tominaga N., Blinnikov S. I., Nomoto K., 2013, *ApJ*, 771, L12
- Tully R. B., 1988, *Nearby Galaxies Catalog*. Cambridge Univ. Press, Cambridge
- Turatto M. et al., 1998, *ApJ*, 498, L129
- Umeda H., Nomoto K., Yamaoka H., Wanajo S., 1999, *ApJ*, 513, 861
- Utrobin V. P., Chugai N. N., 2008, *A&A*, 491, 507
- Utrobin V. P., Chugai N. N., Pastorello A., 2007, *A&A*, 475, 973
- Van Dyk S. D., 2013, *AJ*, 146, 24
- Van Dyk S. D., Li W., Filippenko A. V., 2003, *PASP*, 115, 1289
- Van Dyk S. D. et al., 2012, *AJ*, 143, 19
- Wanajo S., Nomoto K., Janka H.-T., Kitaura F. S., Müller B., 2009, *ApJ*, 695, 208
- Wanajo S., Janka H.-T., Müller B., 2011, *ApJ*, 726, L15

- Wanajo S., Müller B., Janka H.-T., Heger A., 2017, ApJ, preprint (arXiv:1701.06786)
- Wang H., Li J., Wang X. T., Williams C. J., Gould P. L., Stwalley W. C., 1997, Phys. Rev. A, 55, R1569
- Weaver T. A., Zimmerman G. B., Woosley S. E., 1978, ApJ, 225, 1021
- Wongwathanarat A., Müller E., Janka H.-T., 2015, A&A, 577, A48
- Woosley S. E., Heger A., 2007, Phys. Rep., 442, 269
- Woosley S. E., Heger A., 2015, ApJ, 810, 34
- Woosley S. E., Weaver T. A., 1995, ApJS, 101, 181
- Yaron O., Gal-Yam A., 2012, PASP, 124, 668
- Yoshida T., Suwa Y., Umeda H., Shibata M., Takahashi K., 2017, MNRAS, 471, 4275
- Zampieri L., Pastorello A., Turatto M., Cappellaro E., Benetti S., Altavilla G., Mazzali P., Hamuy M., 2003, MNRAS, 338, 711

APPENDIX A: THE PROGENITOR STRUCTURE

Fig. A1 shows the composition, temperature, density and electron fraction in the progenitor. While the progenitor was not calculated here but in Sukhbold et al. (2016), we add this information here for completeness.

APPENDIX B: COMPARISON WITH KEPLER MODEL

Spectra of the KEPLER explosion simulation of the $9 M_{\odot}$ model were also calculated. The density profile of this model compared to the P-HOTB model is plotted in Fig. B1. The KEPLER model shows less dramatic shell compression from β decay than the P-HOTB model. Part of the reason for this is the lower ^{56}Ni mass in KEPLER, $3.6 \times 10^{-3} M_{\odot}$ versus $6.2 \times 10^{-3} M_{\odot}$ in P-HOTB (see table 7 in Sukhbold et al. 2016). The cause of this difference is that the KEPLER simulations lack the neutrino-processed matter ejected from the vicinity of the neutron star after the start of the explosion. The evolution of the reverse shock as it approaches the inner region of the domain also differs between the codes.

The spectra show relatively small differences (Fig. B2). The KEPLER model has a few distinct lines from cobalt emerging at 7540, 9340 and 9950 Å, originating in the core. This is radioactive ^{56}Co , as the abundance of stable cobalt is very low. It also gives a

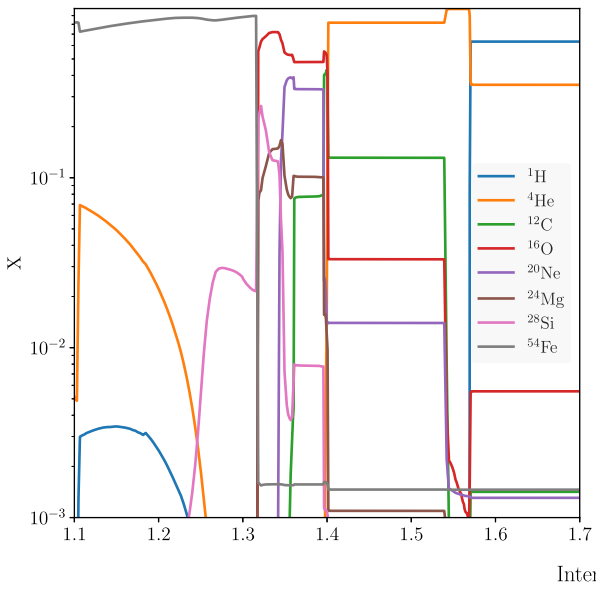


Figure A1. Progenitor model. The left-hand panel shows composition, the upper right density and temperature and the bottom right Y_e .

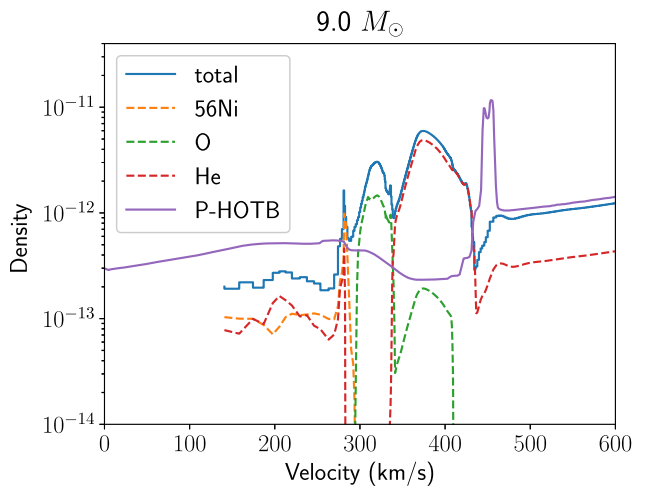


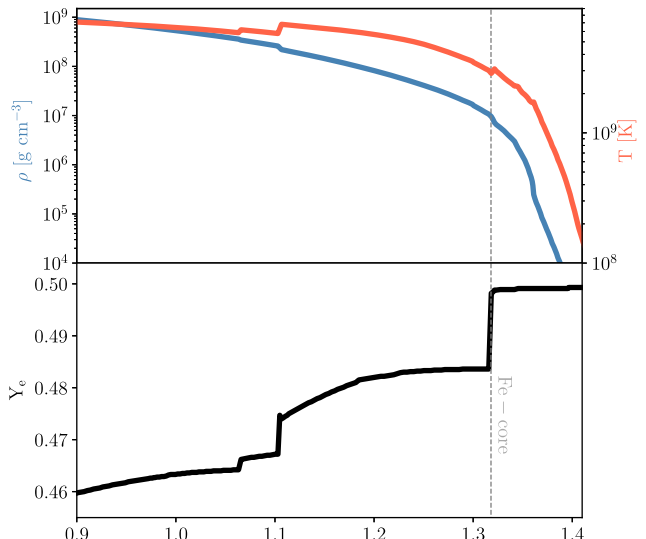
Figure B1. Density profile of the KEPLER model (blue), compared to P-HOTB (purple, see also Fig. 1). The density profiles of He, O and ^{56}Ni are also shown.

stronger [C I] 8727 and Na I D, and weaker calcium lines. The factor ~ 2 variation in these suggest conclusions based on smaller discrepancies with observations than factor 2 should be treated with care. The hydrogen, oxygen, magnesium and iron lines show smaller differences.

Fig. B3 shows a zoom-in on some lines. Whereas lines from the envelope such as H α show little differences in their line profiles, the slower core in the KEPLER model is clearly seen in oxygen, magnesium, and in particular in iron lines.

Nevertheless, it is encouraging for the robustness of the modelling that the differences due to the different explosion methods and nucleosynthesis networks in the two codes are not bigger.

The mass of stable nickel (^{58}Ni and ^{60}Ni) in the KEPLER model (which uses a large nucleosynthesis network) is $1.6 \times 10^{-4} M_{\odot}$, so Ni/Fe = 0.043 (after decay of ^{56}Ni), about the solar value of 0.056 (Lodders 2003). Thus, this explosion simulation shows no continuation of the growing Ni/Fe ratio with declining M_{ZAMS} obtained in the Woosley & Weaver (1995) grid, as illustrated in



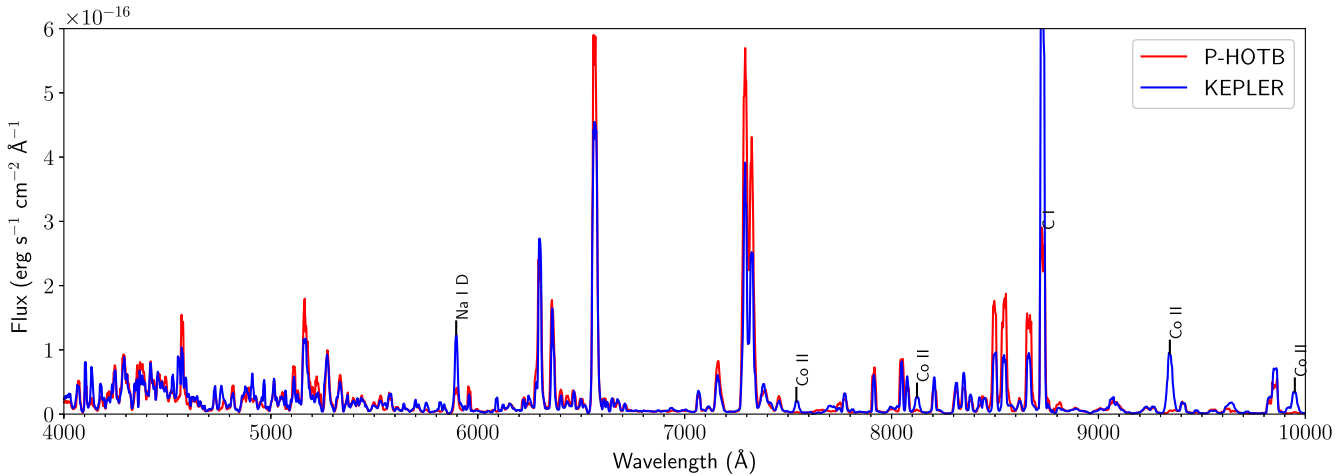


Figure B2. Comparison of P-HOTB (red) and KEPLER (blue) model spectra at 400d. The models have been scaled to have the same ^{56}Ni mass, and convolved with a Gaussian of FWHM = 150 km s $^{-1}$. The lines showing the biggest difference are labelled.

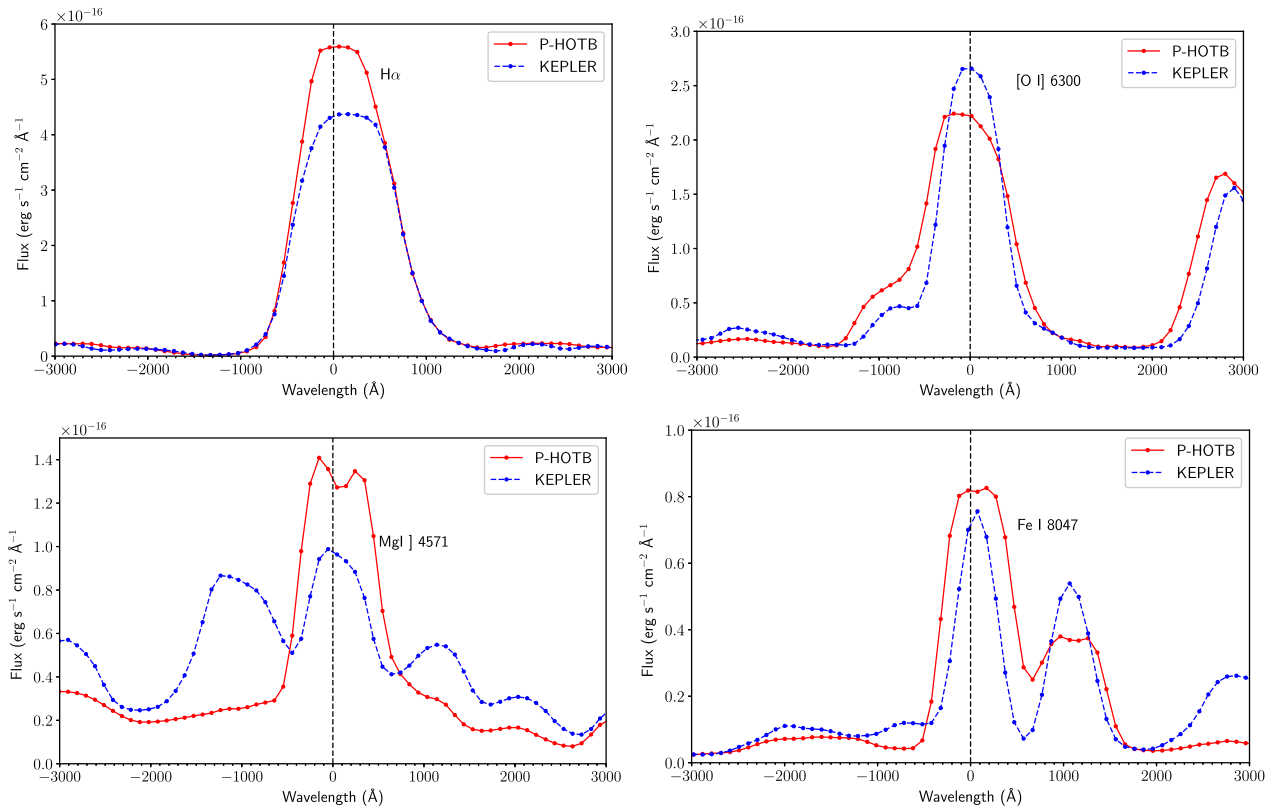


Figure B3. Comparison of selected line profiles in P-HOTB (red, solid) and KEPLER (blue, dashed) at 400d.

fig. 8 of Jerkstrand et al. (2015c). The mass cut is at $1.35 M_{\odot}$, which is in the oxygen shell, where $Y_e \sim 0.499$ and where solar Ni/Fe production occurs. The KEPLER simulations also lack the neutrino processing that gives rise to neutron-rich production in the inner layers.

APPENDIX C: COMPOSITION MAPPING

One limitation of Eulerian explosion simulations like P-HOTB is that compositionally distinct layers get artificially mixed as they are ‘cut’ by the Eulerian spatial gridding at each time-step. The

final composition profiles of a model at late time are significantly different than at early time. Fig. C1 compares composition at 2s and 100d, showing the effect.

For the computed models, the composition versus mass coordinate was taken at 2s. Material inside $1.35803 M_{\odot}$ in the $9 M_{\odot}$ model is still evolving at 2s (see Fig. C1, bottom panel), processing of another $0.0067 M_{\odot}$ will increase the total ^{56}Ni yield from $5.0 \times 10^{-3} M_{\odot}$ at 2s to a final $6.2 \times 10^{-3} M_{\odot}$. To include this, the composition in this innermost region (1.35138 – $1.35803 M_{\odot}$) was taken from the 100d model rather than the 2s model.

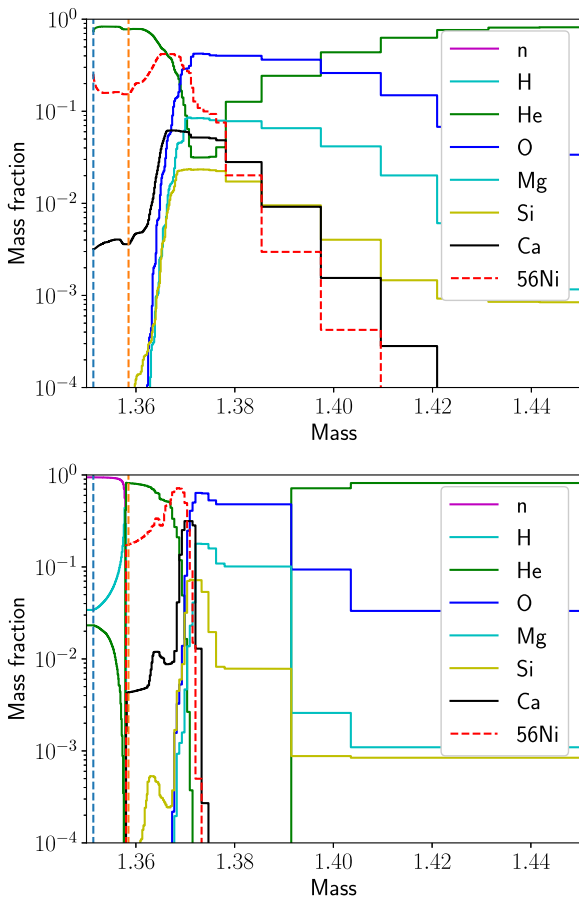


Figure C1. Illustration of numeric diffusion of composition. The top panel shows composition versus mass coordinate in a simulation run to 100d. The bottom shows a run to 2 s. The left-most vertical line at $1.35138 M_{\odot}$ denotes the ‘mass cut’ (taken as $V > 50 \text{ km s}^{-1}$ at 100d). The second vertical line at $1.35803 M_{\odot}$ marks the mass coordinate inside which the composition is n and p at 2s (not yet assembled to ^{56}Ni).

In the 2 s model, ^{56}Ni extends only into a small fraction of the O shell (~ 10 per cent by mass). Nevertheless, the O shell is moving at only a slightly higher velocity ($\sim 25 \text{ km s}^{-1}$) than the ^{56}Ni -rich shell at $1.36\text{--}1.37 M_{\odot}$. Therefore, with limited velocity resolution

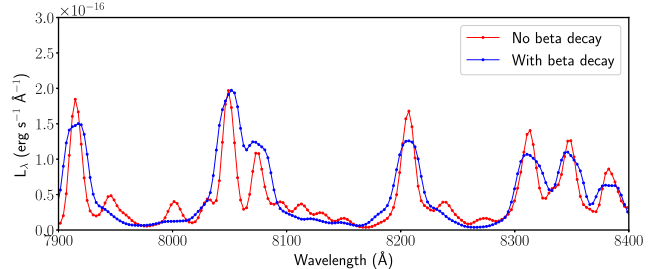


Figure D2. Zoom-in of Fig. D1 on the $7900\text{--}8500 \text{\AA}$ region. Here, a telescope convolution of 300 km s^{-1} has also been added.

(10 km s^{-1}), ^{56}Ni gets mixed into about half of the O-rich region in our grid (Fig. 2). Binning has to be finer than 5 or maximum 10 km s^{-1} to resolve the individual composition shells. Beyond some limit, increased velocity resolution will become meaningless as several physical processes treated in on-the-spot approximations in the model occur in reality over some finite volume/velocity dispersion. What exactly these volume scales are would require a detailed separate investigation.

APPENDIX D: SENSITIVITY TO RADIOACTIVE DECAY

We study here the impact of the ‘ ^{56}Ni bubble’ for the spectral formation. This long-term dynamic evolution of the ejecta is often ignored in explosion simulations and spectral models, so it is of interest to improve an understanding of its significance.

Fig. D1 compares models computed with and without the dynamic effect of radioactivity on the ejecta, at 300d. Fig. 1 compares the density profiles for the two cases. The factor ~ 2 larger core velocities in the model with decay leads to broader lines and less fine-structure in the spectrum. The overall spectral properties are not much changes, but some lines show sensitivity.

Fig. D2 shows a zoom-in on the $7900\text{--}8500 \text{\AA}$ region, where also convolution to 300 km s^{-1} has been applied to simulate an actual observation. The difference in width of Fe lines can also be seen after this convolution.

Regarding line luminosities, the beta decay model has in particular increased the brightness in $\text{H}\alpha$, and reduced the brightness in $[\text{C}\,\text{i}] 8727$ (factor 2). The reduced column density of the He core leads to more gamma-rays escaping into the H envelope,

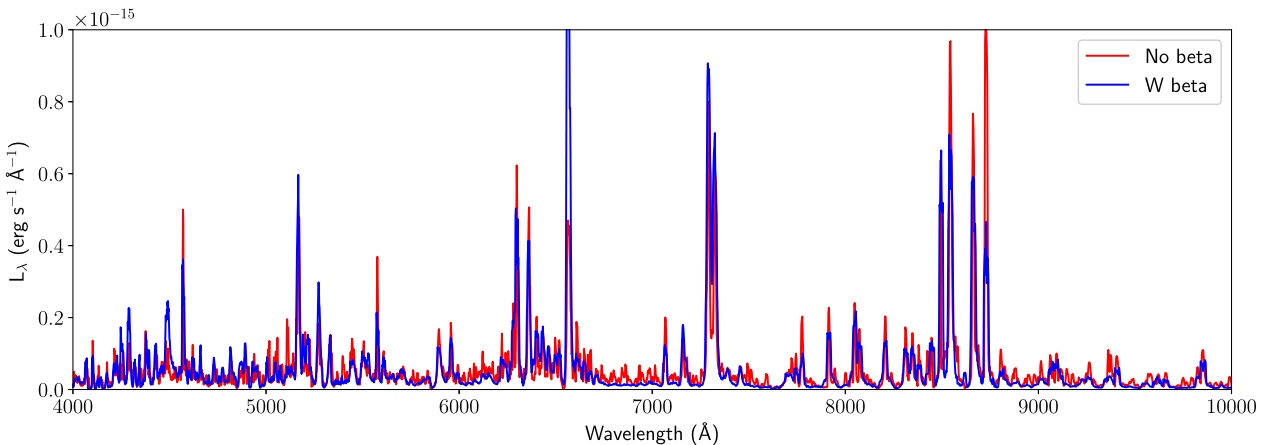


Figure D1. Comparison for the $9 M_{\odot}$ model without (red) and with (blue) dynamic effects of beta decay, at 300d. The beta decay broadens the lines and changes some luminosities significantly, e.g. in $\text{H}\alpha$ and $[\text{C}\,\text{i}] 8727$.

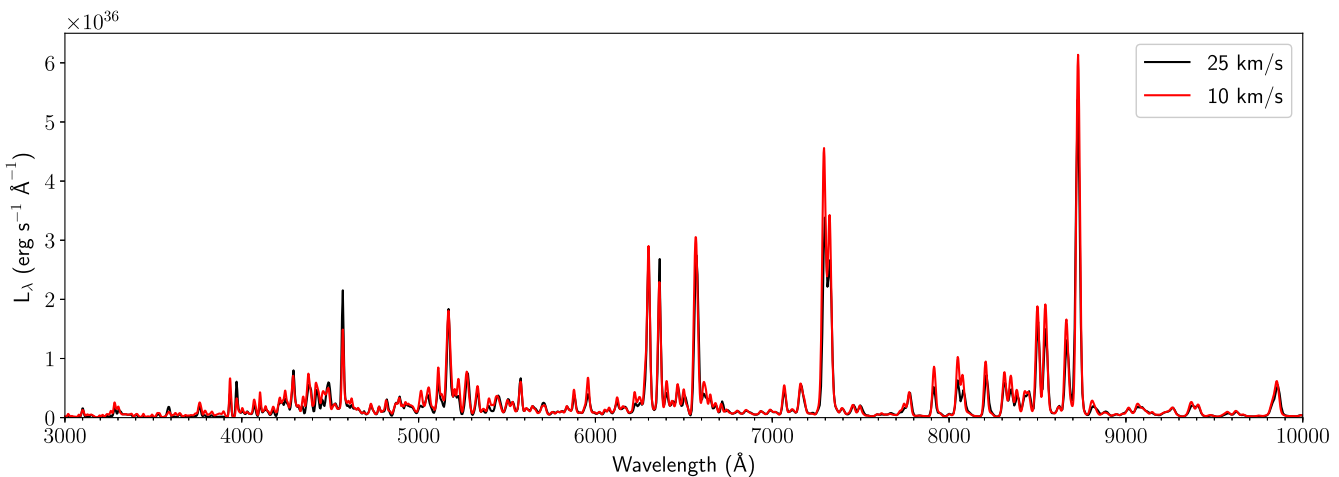


Figure E1. Comparison between using 10 (red) and 25 (black) km s^{-1} zoning ($9 M_\odot$ models at 400d, excluding ^{56}Ni dynamics). A 25 km s^{-1} zoning is fully converged.

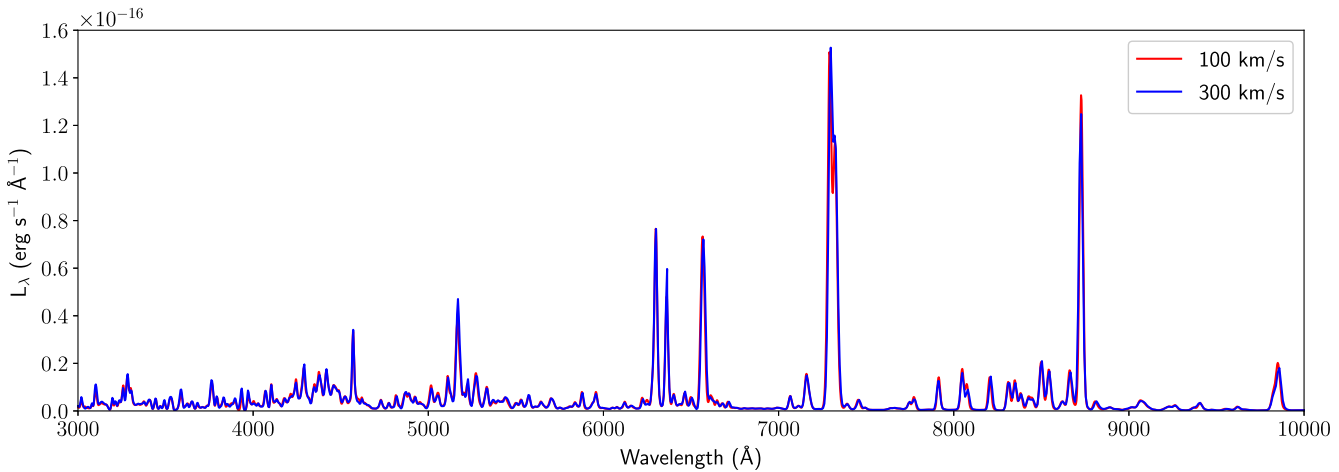


Figure F1. Sensitivity test to frequency resolution ($9 M_\odot$ model (excluding ^{56}Ni dynamics) at 500d). A 300 km s^{-1} resolution is fully converged.

producing the boosted $H\alpha$ effect. At 300d, the deposition in the four main zones is 35–35–25–5 per cent in the model without decay, and 20–15–40–30 per cent in the model with decay. The marginally optically thin Ni and O shells show a factor ~ 2 drop in absorption (expected as V^{-2} in the optically thin limit, and here their V increase by a factor ~ 1.5), and this energy instead goes into the He shell and optically thick H envelope. In that sense, the decay mimics the effect of macroscopic mixing of H into the He core.

However, not all lines show a simple behaviour. The Fe I lines, and also [O I] 6300, 6364 remain mostly unchanged, despite a factor 2 lower energy deposition in the core zones. This illustrates the complexity of the spectral formation, where radiative cross-talk, optical depth effects and changing ionization balance all can play a role. The extreme compression of the O/He shells in the beta decay model also leads to some compositional mixing.

APPENDIX E: SENSITIVITY TO ZONING/VELOCITY RESOLUTION

The composition of the core changes on relatively small velocity scales, of order 10 km s^{-1} in the O layer (Fig. 2). As the emission spectrum can change quite dramatically depending on details

of composition, it is important to ensure that the simulations are converged with regard to velocity resolution (zoning).

Fig. E1 compares spectra computed with 10 and 25 km s^{-1} in the core (models with no beta decay). There are almost no differences, which demonstrates that zoning is sufficient.

APPENDIX F: SENSITIVITY TO FREQUENCY RESOLUTION

Fig. F1 shows a comparison of models using $R (= \lambda/\Delta\lambda) = 1000$ (300 km s^{-1} bins) and $R = 3000$ (100 km s^{-1}), for the $9 M_\odot$ model at 500d. No discernible differences are obtained for either line luminosities or spectral form. This shows that unless one needs very specific line profiles, $R = 1000$ is sufficient for the modelling. Our standard resolution is $R = 3000$.

APPENDIX G: ATOMIC DATA UPDATE

We have updated atomic data for Mg I with the new collision strength values from Barklem et al. (2017). The old values used were from Mauas, Avrett & Loeser (1988).

K I has been added to the code as a 3-level atom (with the purpose to be able to model the K I 7665, 7699 ground state scattering line).

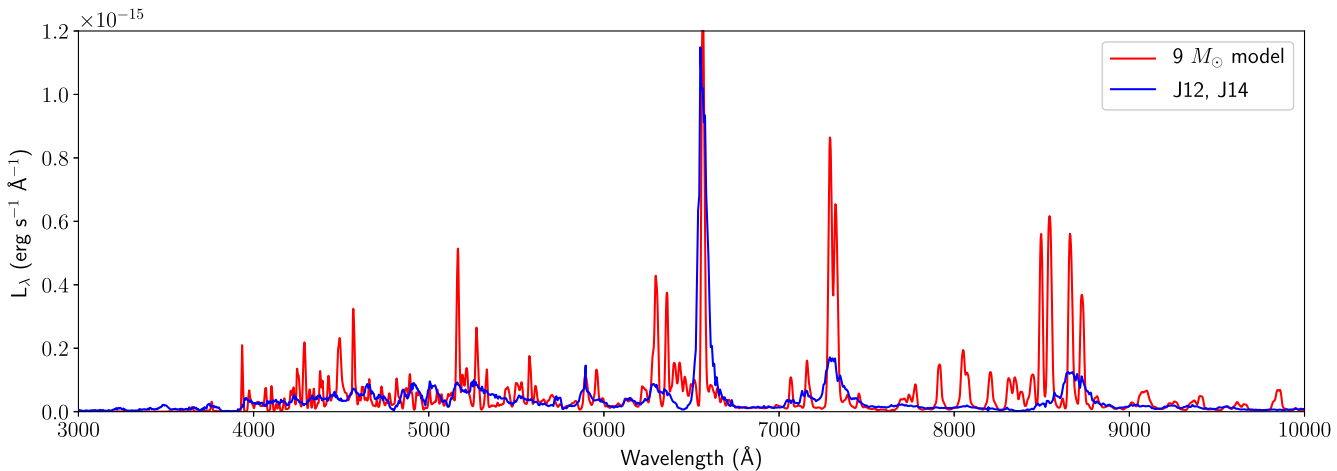


Figure H1. Comparison of $9 M_{\odot}$ model (red) with the $12 M_{\odot}$ model in J12/J14 (blue), at 300d.

Level energies and A -values from Wang et al. (1997) and Falke et al. (2006).

APPENDIX H: RELATION TO J12/J14 MODELS

J12, J14 computed Type IIP models for the $12\text{--}25 M_{\odot}$ progenitor range. These models differed not only in what M_{ZAMS} was used, but also in the explosion energy (1.2 B), nucleosynthesis (larger network employed), explosion method (piston), artificial mixing and parameterised molecule cooling was employed. It is nevertheless interesting to investigate the relation between the new models and the ones in J12/J14.

Fig. H1 compares the $9 M_{\odot}$ model computed here with the $12 M_{\odot}$ model in J14 at 300d. The spectra are rescaled with the difference in ^{56}Ni mass, and the J14 model has also been compensated at the 10 per cent level for its dust content. The spectra have relatively similar colours. The obvious difference is the much narrower lines in the $9 M_{\odot}$ model. For line luminosities, the $[\text{O I}] + \text{Fe I}$ blend is stronger in the $9 M_{\odot}$ model than in the $12 M_{\odot}$ model, despite a higher O mass in the $12 M_{\odot}$ model. This effect presumably arises as the O shell in the $9 M_{\odot}$ model lies closer to the ^{56}Ni in the unmixed set-up, the $9 M_{\odot}$ model lacks molecular cooling, and there is also significant Fe I contribution to the 6364 line (but 6300 is mostly [O I]).

The most distinct qualitative differences are the Fe I lines in the $7900\text{--}8500 \text{\AA}$ region; these are not produced in the J12/J14 models. In those models, the strong mixing and clumping (treated in 1D by the method of ‘virtual gridding’; see Jerkstrand, Fransson & Kozma 2011) of the core give only 7 per cent gamma deposition in the ^{56}Ni clumps at 300d, compared to 20 per cent in the unmixed $9 M_{\odot}$ model. Lower velocities combine with higher energy deposition in the Fe zone to make more distinct Fe lines (happens also for e.g. [Fe II] 7155). For the O zone, the J12/J14 models use parametrized molecular cooling in the O/Si/S and O/C zones, which removes about 2/3 of the O shell optical emission, effectively giving a lower power level for [O I] than in the $9 M_{\odot}$ model. As stated before, in the optically thick regime the morphology, e.g. structure and proximity to the ^{56}Ni , is as important as the mass of a zone in determining its line luminosities. Only for ‘all else constant’ does a higher zone mass lead to higher emission. In this comparison both zone masses and morphology are different, and the morphological differences often dominate.

The lack of many trace metals in the new models may also influence the spectra, in particular the blue regions, where reduced line blocking may overestimate the blue emergent flux.

APPENDIX I: OBSERVATIONAL COMPARISON BETWEEN SUBLUMINOUS AND NORMAL SNE

Fig. I1 compares SN 2005cs at +277d with ‘normal’ IIP SN 2012aw at +250d. The main qualitative differences are the clear Fe I lines in the $8000\text{--}9500 \text{\AA}$ window in SN 2005cs. There are hints of bumps at all of these also in SN 2012aw, but some combination of higher velocities and lower intrinsic brightness makes them less distinct. The higher velocities on SN 2012aw are made clear from the absorption troughs of Na I D, K I 7699, Ca II 8498 (which eats up O I 8446), and narrower emission profiles in e.g. H α . It is clear that the velocity of the emitting region at nebular times is a factor 1.5–2 smaller in SN 2005cs than in SN 2012aw. This must invariably be linked to the (bulk of) ^{56}Ni distribution being at a factor ~ 2 lower velocities.

Although we do not have access to the data, we can from fig. 13 in Lisakov et al. (2017) comment on the similarity between SN 2005cs and SN 2008bk at +280d. The spectra are largely similar, although

- (i) SN 2008bk shows a clear He I 7065, but a weaker [C I] 8727.
- (ii) [Ca II] 7300 is doubly peaked in SN 2008bk, and lacks the red tail of SN 2005cs.
- (iii) SN 2008bk shows a larger number of matching Fe I lines, including 7900 and 8400 \AA . This may relate to its factor 2 higher ^{56}Ni mass.

All in all this comparison makes it clear that it would be difficult to argue that SN 2005cs and SN 2008bk would have any fundamental differences. But that argument also implies that our model, for some reason, is not giving very accurate output for this epoch. We note that the best matches for SN 1997D and SN 2008bk were for +350, +484 and +513d. The +207d spectrum of SN 1997D fits well from H α and redwards, but there are discrepancies in the blue. Thus, there may be some issues in the model that makes the blue region inaccurate at early epochs $t \lesssim 300$ d.

Finally, Fig. I2 compares SN 1997D and SN 2005cs at around 200d. The extreme lack of line structure in SN 2005cs at blue wavelengths is highlighted.

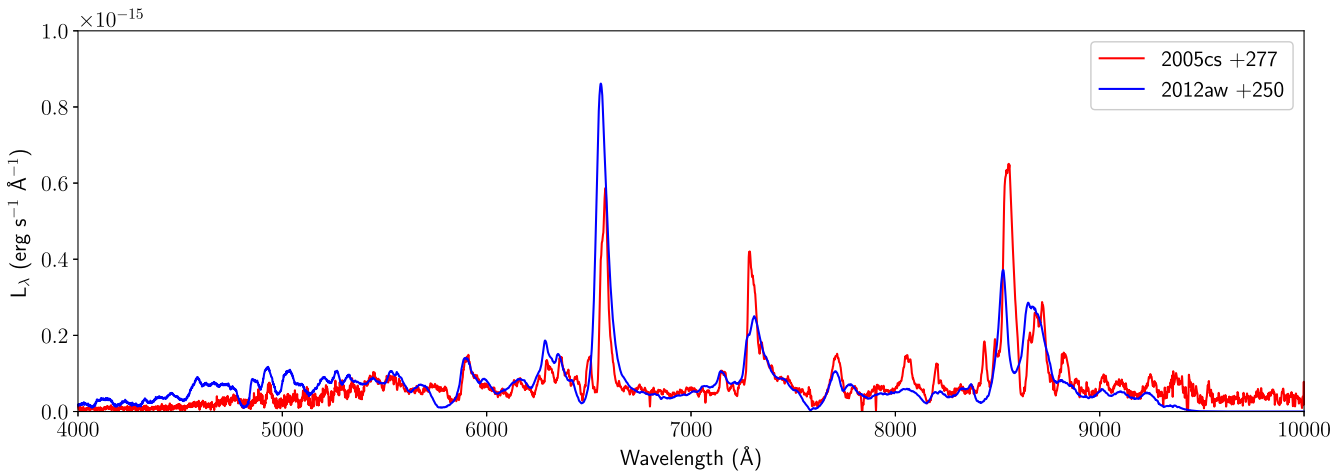


Figure I1. SN 2005cs (red) compared to SN 2012aw (blue), at about 260d. SN 2005cs has lower velocities, and more pronounced Fe I lines at 7900–8500 Å. Note the similarity in the red wing of [Ca II].

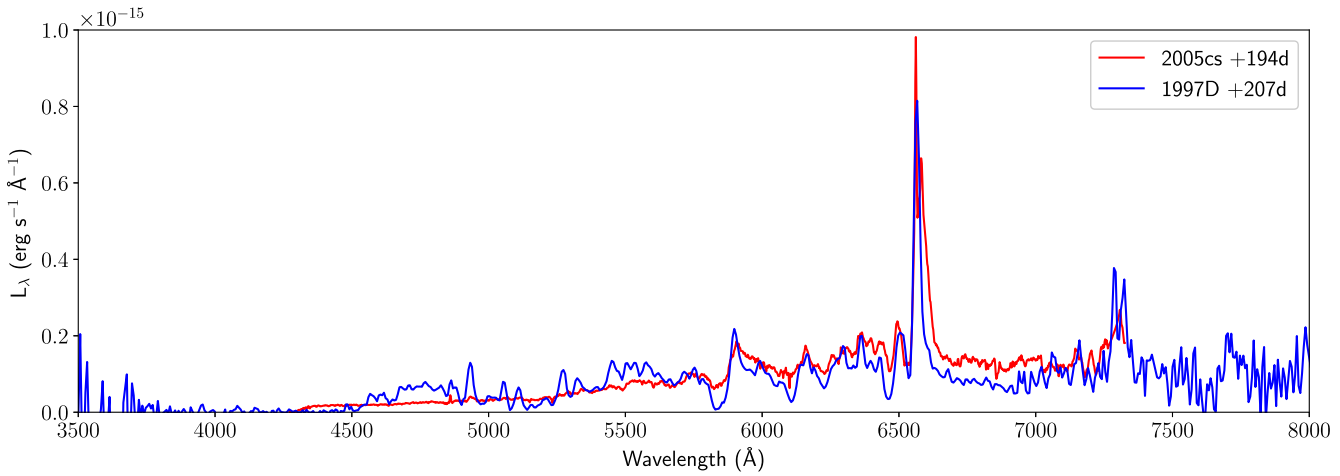


Figure I2. SN 1997D (blue) compared to SN 2005cs (red), at around 200d.

This paper has been typeset from a $\text{\TeX}/\text{\LaTeX}$ file prepared by the author.